A Geometric View of Data Complexity: Efficient Local Intrinsic Dimension Estimation with Diffusion Models

Hamidreza Kamkari [1] Brendan Leigh Ross [1] Rasa Hosseinzadeh [1] Jesse C. Cresswell [1] Gabriel Loaiza-Ganem [1]

Abstract

High-dimensional data commonly lies on low-dimensional submanifolds, and estimating the *local intrinsic dimension* (LID) of a datum – i.e. the dimension of the submanifold it belongs to – is a longstanding problem. LID can be understood as the number of local factors of variation: the more factors of variation a datum has, the more complex it tends to be. Estimating this quantity has proven useful in contexts ranging from generalization in neural networks to detection of out-of-distribution data, adversarial examples, and AI-generated text. The recent successes of deep generative models present an opportunity to leverage them for LID estimation, but current methods based on generative models produce inaccurate estimates, require more than a single pre-trained model, are computationally intensive, or do not exploit the best available deep generative models, i.e. diffusion models (DMs). In this work, we show that the Fokker-Planck equation associated with a DM can provide a LID estimator which addresses all the aforementioned deficiencies. Our estimator, called FLIPD, is compatible with all popular DMs, and outperforms existing baselines on LID estimation benchmarks. We also apply FLIPD on natural images where the true LID is unknown. Compared to competing estimators, FLIPD exhibits higher correlation with non-LID measures of complexity, better matches a qualitative assessment of complexity, and is the only estimator to remain tractable with high-resolution images at the scale of Stable Diffusion.

[*]Equal contribution [1]Layer 6 AI, Toronto, Canada. Correspondence to: Hamidreza Kamkari <hamid@layer6.ai>.

Accepted by the Structured Probabilistic Inference & Generative Modeling workshop of ICML 2024, Vienna, Austria. Copyright 2024 by the author(s).

1. Introduction

The manifold hypothesis (Bengio et al., 2013), which has been empirically verified in contexts ranging from natural images (Pope et al., 2021; Brown et al., 2023) to calorimeter showers in physics (Cresswell et al., 2022), states that high-dimensional data of interest in $\mathbb{R}^D$ often lies on low-dimensional submanifolds of $\mathbb{R}^D$. For a given datum $x \in \mathbb{R}^D$, this hypothesis motivates using its *local intrinsic dimension* (LID), denoted $\text{LID}(x)$, as a natural measure of its complexity. $\text{LID}(x)$ corresponds to the dimension of the data manifold that x belongs to, and can be intuitively understood as the minimal number of variables needed to describe x. More complex data needs more variables to be adequately described, as illustrated in Figure 1. Data manifolds are typically not known explicitly, meaning that LID must be estimated. Here we tackle the following problem: given a dataset along with a query datum x, how can we tractably estimate $\text{LID}(x)$?

This is a longstanding problem, with LID estimates being highly useful due to their innate interpretation as a measure of complexity. For example, these estimates can be used to detect outliers (Houle et al., 2018; Anderberg et al., 2024; Kamkari et al., 2024b), AI-generated text (Tulchinskii et al., 2023), and adversarial examples (Ma et al., 2018). Connections between a neural network's generalization capabilities and the LID estimates of its internal representations have also been shown (Ansuini et al., 2019; Birdal et al., 2021; Magai & Ayzenberg, 2022; Brown et al., 2022). These insights can be leveraged to identify which representations contain maximal semantic content (Valeriani et al., 2023), and help explain why LID estimates can be helpful as regularizers (Zhu et al., 2018) and for pruning large models (Xue et al., 2022). LID estimation is thus not only of mathematical and statistical interest, but can also benefit the empirical performance of deep learning models at numerous tasks.

Traditional estimators of intrinsic dimension (Fukunaga & Olsen, 1971; Levina & Bickel, 2004; MacKay & Ghahramani, 2005; Cangelosi & Goriely, 2007; Johnsson et al., 2014; Facco et al., 2017; Albergante et al., 2019; Bac et al., 2021) typically rely on pairwise distances and nearest neighbours, so computing them is prohibitively expensive for large datasets. Recent work has thus sought to move away

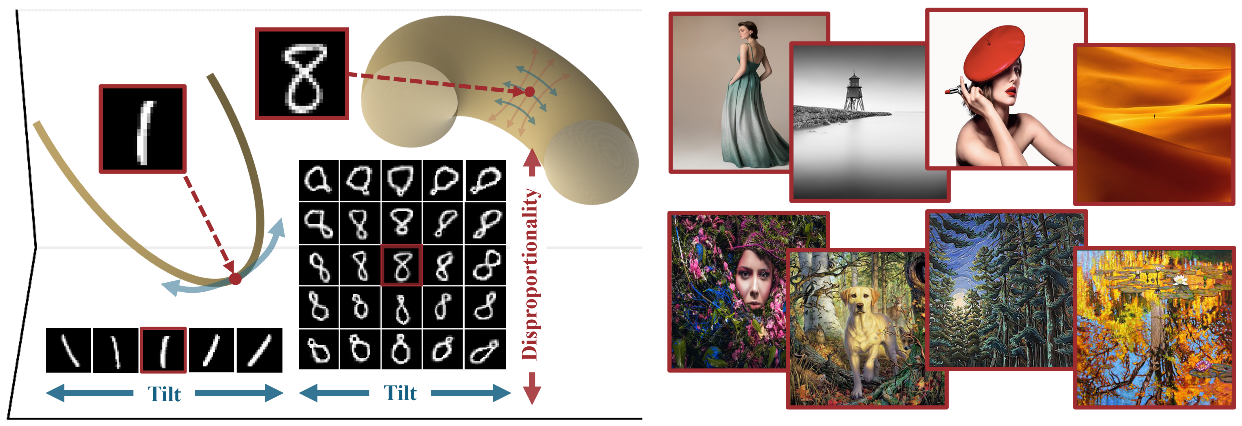

Figure 1: **(Left)** A cartoon illustration showing that LID is a natural measure of relative complexity. We depict two manifolds of MNIST digits, corresponding to 1s and 8s, as 1-dimensional and 2-dimensional submanifolds of $\mathbb{R}^3$, respectively. The relatively simpler manifold of 1s exhibits a single factor of variation ("tilt"), whereas 8s have an additional factor of variation ("disproportionality"). **(Right)** The 4 lowest- and highest-LID datapoints from a subsample of LAION Aesthetics, as measured by our method, FLIPD, applied to Stable Diffusion v1.5. FLIPD scales efficiently to large models on high-dimensional data, and aligns closely with subjective complexity.

from these *model-free* estimators and instead take advantage of deep generative models which learn the distribution of observed data. When this distribution is supported on low-dimensional submanifolds of $\mathbb{R}^D$, successful generative models must implicitly learn the dimensions of the data submanifolds, suggesting they can be used to construct LID estimators. However, existing *model-based* estimators suffer from various drawbacks, including being inaccurate and computationally expensive (Stanczuk et al., 2022), not leveraging the best existing generative models (Tempczyk et al., 2022; Zheng et al., 2022) (i.e. diffusion models (Sohl-Dickstein et al., 2015; Ho et al., 2020; Song et al., 2021b)), and requiring training several models (Tempczyk et al., 2022) or altering the training procedure rather than relying on a pre-trained model (Horvat & Pfister, 2024). None of these methods scale to high-resolution images such as those generated by Stable Diffusion (Rombach et al., 2022).

We address all these issues by showing how to estimate LID efficiently using only a single pre-trained diffusion model (DM) by building on LIDL (Tempczyk et al., 2022), a model-based estimator. LIDL operates by convolving data with different levels of Gaussian noise, training a normalizing flow (Rezende & Mohamed, 2015; Dinh et al., 2017; Durkan et al., 2019) for each level, and fitting a linear regression using the log standard deviation of the noise as a covariate and the corresponding log density (of the convolution) evaluated at x as the response; the resulting slope is an estimate of $\text{LID}(x) - D$, thanks to a surprising result linking Gaussian convolutions and LID. We first show how to adapt LIDL to DMs in a way that only a single DM is required (rather than many normalizing flows). Directly applying this insight leads to LIDL estimates that require one DM but several calls to an ordinary differential equation (ODE) solver; we also show how to sidestep this with an alternative ODE that computes all the required log densities in a single solve. We then argue that the slope of the regression in LIDL aims to capture a rate of change which, for DMs, can be evaluated directly thanks to the Fokker-Planck equation. The resulting estimator, which we call FLIPD,[1] is highly efficient and circumvents the need for an ODE solver.

Our contributions are: (i) showing how DMs can be efficiently combined with LIDL in a way which requires a single call to an ODE solver; (ii) leveraging the Fokker-Planck equation to propose FLIPD, thus improving upon the estimator and circumventing the need for an ODE solver altogether; (iii) motivating FLIPD theoretically; (iv) introducing a suite of LID estimation benchmark tasks highlighting that the previously reported good performance of other estimators is due in part to the simplicity of the tasks over which they were evaluated; (v) demonstrating that FLIPD tends to outperform existing baselines, particularly in high-dimensional settings, while being much more computationally efficient – FLIPD is the first LID estimator to scale to high-resolution images ($\sim 10^6$ dimensions), and can be used with Stable Diffusion; and (vi) showing that when applied to natural images, compared to competing alternatives, FLIPD is more aligned both with other measures of complexity such as PNG compression length, and with qualitative assessments of complexity.

[1]Pronounced as "flipped", the acronym is a rearrangement of "FP" from Fokker-Planck and "LID".

2. Background and Related Work

2.1. Diffusion Models

Forward and backward processes Diffusion models admit various formulations (Sohl-Dickstein et al., 2015; Ho et al., 2020); here we follow the score-based one (Song et al., 2021b). We denote the true data-generating distribution, which DMs aim to learn, as $p(\cdot, 0)$. DMs define the forward (Itô) stochastic differential equation (SDE),

$$\mathrm{d}X_t = f(X_t, t)\mathrm{d}t + g(t)\mathrm{d}W_t, \quad X_0 \sim p(\cdot, 0), \qquad (1)$$

where $f : \mathbb{R}^D \times [0,1] \to \mathbb{R}^D$ and $g : [0,1] \to \mathbb{R}$ are hyperparameters, and W_t denotes a D-dimensional Brownian motion. We write the distribution of X_t as $p(\cdot, t)$. The SDE in Equation 1 prescribes how to gradually add noise to data, the idea being that $p(\cdot, 1)$ is essentially pure noise. Defining the backward process as $Y_t \coloneqq X_{1-t}$, this process obeys the backward SDE (Anderson, 1982; Haussmann & Pardoux, 1986),

$$\begin{aligned}\mathrm{d}Y_t = &\left[g^2(1-t)s(Y_t, 1-t) - f(Y_t, 1-t)\right]\mathrm{d}t \\ &+ g(1-t)\mathrm{d}\hat{W}_t,\ Y_0 \sim p(\cdot, 1),\end{aligned} \qquad (2)$$

where $s(x, t) \coloneqq \nabla \log p(x, t)$ is the unknown (Stein) score function,[2] and $\hat{W}_t$ is another D-dimensional Brownian motion. DMs leverage this backward SDE for generative modelling by using a neural network $\hat{s} : \mathbb{R}^D \times (0,1] \to \mathbb{R}^D$ to learn the score function with denoising score matching (Vincent, 2011). Once trained, $\hat{s}(x,t) \approx s(x,t)$. To generate samples $\hat{Y}_1$ from the model, we solve an approximation of Equation 2:

$$\begin{aligned}\mathrm{d}\hat{Y}_t = &\left[g^2(1-t)\hat{s}(\hat{Y}_t, 1-t) - f(\hat{Y}_t, 1-t)\right]\mathrm{d}t \\ &+ g(1-t)\mathrm{d}\hat{W}_t,\ \hat{Y}_0 \sim \hat{p}(\cdot, 1),\end{aligned} \qquad (3)$$

with $\hat{s}$ replacing the true score and with $\hat{p}(\cdot, 1)$, a Gaussian distribution chosen to approximate $p(\cdot, 1)$ (depending on f and g), replacing $p(\cdot, 1)$.

Density Evaluation DMs can be interpreted as continuous normalizing flows (Chen et al., 2018), and thus admit density evaluation, meaning that if we denote the distribution of $\hat{Y}_{1-t}$ as $\hat{p}(\cdot, t)$, then $\hat{p}(x, t_0)$ can be mathematically evaluated for any given $x \in \mathbb{R}^D$ and $t_0 \in (0, 1]$. More specifically, this is achieved thanks to the (forward) ordinary differential equation (ODE) associated with the DM:

$$\mathrm{d}\hat{x}_t = \left(f(\hat{x}_t, t) - \frac{1}{2}g^2(t)\hat{s}(\hat{x}_t, t)\right)\mathrm{d}t, \quad \hat{x}_{t_0} = x. \qquad (4)$$

[2]Throughout this paper, we use the symbol ∇ to denote the differentiation operator with respect to the vector-valued input, not the scalar time t, i.e. $\nabla = \partial/\partial x$.

Solving this ODE from time t_0 to time 1 produces the trajectory $(\hat{x}_t)_{t\in[t_0,1]}$, which can then be used for density evaluation through the continuous change-of-variables formula:

$$\log \hat{p}(x, t_0) = \log \hat{p}(\hat{x}_1, 1) + \int_{t_0}^{1} \mathrm{tr}(\nabla v(\hat{x}_t, t))\mathrm{d}t, \qquad (5)$$

where $\hat{p}(\cdot, 1)$ can be evaluated since it is a known Gaussian, and where $v(x, t) \coloneqq f(x, t) - g^2(t)\hat{s}(x, t)/2$.

Trace estimation The cost of computing $\nabla v(\hat{x}_t, t)$ for a particular $\hat{x}_t$ amounts to $\mathcal{O}(D)$ function evaluations of $\hat{s}$ (since D calls to a Jacobian-vector-product routine are needed (Baydin et al., 2018)). Although this is not prohibitively expensive for a single $\hat{x}_t$, in order to compute the integral in Equation 5 in practice, $(\hat{x}_t)_{t\in[t_0,1]}$ must be discretized into a trajectory of length N. Deterministic density evaluation is thus computationally intractable as it costs $\mathcal{O}(ND)$ function evaluations. The Hutchinson trace estimator (Hutchinson, 1989) – which states that for $M \in \mathbb{R}^{D\times D}$, $\mathrm{tr}(M) = \mathbb{E}_\varepsilon[\varepsilon^\top M \varepsilon]$, where $\varepsilon \in \mathbb{R}^D$ has mean 0 and covariance I_D – is thus commonly used for stochastic density estimation; approximating the expectation with k samples from ε results in a cost of $\mathcal{O}(Nk)$, which is much faster than deterministic density evaluation when $k \ll D$.

2.2. Local Intrinsic Dimension and How to Estimate It

LID Various definitions of intrinsic dimension exist (Hurewicz & Wallman, 1948; Falconer, 2007; Lee, 2012), here we follow the standard one from geometry: a d-dimensional manifold is a set which is locally homeomorphic to $\mathbb{R}^d$. For a given disjoint union of manifolds and a point x in this union, the *local intrinsic dimension* of x is the dimension of the manifold it belongs to. Note that LID is not an intrinsic property of the point x, but rather a property of x with respect to the manifold that contains it. Intuitively, LID(x) corresponds to the number of factors of variation present in the manifold containing x, and it is thus a natural measure of the relative complexity of x, as illustrated in Figure 1.

Estimating LID As previously mentioned, the natural interpretation of LID as a measure of complexity makes estimating it from observed data a relevant problem. Here, the formal setup is that $p(\cdot, 0)$ is supported on a disjoint union of manifolds (Brown et al., 2023), and we assume access to a dataset sampled from it. Then, for a given x in the support of $p(\cdot, 0)$, we want to use the dataset to provide an estimate of LID(x). Traditional estimators (Fukunaga & Olsen, 1971; Levina & Bickel, 2004; MacKay & Ghahramani, 2005; Cangelosi & Goriely, 2007; Johnsson et al., 2014; Facco et al., 2017; Albergante et al., 2019; Bac et al., 2021) rely on the nearest neighbours of x in the dataset, or related quantities, and typically have quadratic scaling on dataset size. Generative models are an intuitive alternative to these methods; because they are trained to learn $p(\cdot, 0)$, when they succeed they must encode information about the support of $p(\cdot, 0)$, including the corresponding manifold dimensions. However, extracting this information from a trained generative model is not trivial. For example, Zheng et al. (2022) showed that the number of active dimensions in the approximate posterior of variational autoencoders (Kingma & Welling, 2014; Rezende & Mohamed, 2015) estimates LID, but their approach does not generalize to better generative models.

LIDL Tempczyk et al. (2022) proposed LIDL, a method for LID estimation relying on normalizing flows (Rezende & Mohamed, 2015; Dinh et al., 2017; Durkan et al., 2019). LIDL works thanks to a surprising result linking Gaussian convolutions and LID (Loaiza-Ganem et al., 2022; Tempczyk et al., 2022; Zheng et al., 2022). We will denote the convolution of $p(\cdot, 0)$ and Gaussian noise with log standard deviation δ as $\varrho(\cdot, \delta)$, i.e.

$$\varrho(x, \delta) \coloneqq \int p(x_0, 0)\mathcal{N}(x - x_0; 0, e^{2\delta} I_D)\mathrm{d}x_0. \tag{6}$$

The aforementioned result states that, under mild regularity conditions on $p(\cdot, 0)$, and for a given x in its support, the following holds as $\delta \to -\infty$:

$$\log \varrho(x, \delta) = \delta(\mathrm{LID}(x) - D) + \mathcal{O}(1). \tag{7}$$

This result then suggests that, for negative enough values of δ (i.e. small enough standard deviations):

$$\log \varrho(x, \delta) \approx \delta(\mathrm{LID}(x) - D) + c \tag{8}$$

for some constant c. If we could evaluate $\log \varrho(x, \delta)$ for various values of δ, this would provide an avenue for estimating $\mathrm{LID}(x)$: set some values $\delta_1, \dots, \delta_m$, fit a linear regression using $\{(\delta_i, \log \varrho(x, \delta_i))\}_{i=1}^m$ (with δ as the covariate and $\log \varrho(x, \delta)$ as the response), and let $\hat{\beta}_x$ be the corresponding slope. It follows that $\hat{\beta}_x$ estimates $\mathrm{LID}(x) - D$, so that $\mathrm{LID}(x) \approx D + \hat{\beta}_x$ is a sensible estimator of local intrinsic dimension.

Since $\varrho(x, \delta)$ is unknown, LIDL requires training m normalizing flows. More specifically, for each δ_i, a normalizing flow is trained on data to which $\mathcal{N}(0, e^{2\delta_i} I_D)$ noise is added. In LIDL, the log densities of the trained models are then used instead of the unknown true log densities $\log \varrho(x, \delta_i)$ when fitting the regression as described above.

Despite using generative models, LIDL has obvious drawbacks. LIDL requires training several models. It also relies on normalizing flows, which are not only empirically outperformed by DMs by a wide margin, but are also known to struggle to learn low-dimensional manifolds (Cornish et al., 2020; Loaiza-Ganem et al., 2022; 2024). On the other hand, DMs do not struggle to learn $p(\cdot, 0)$ even when it is supported on low-dimensional manifolds (Pidstrigach, 2022; De Bortoli, 2022; Loaiza-Ganem et al., 2024), further suggesting that LIDL can be improved by leveraging DMs.

Estimating LID with DMs The only works we are aware of that leverage DMs for LID estimation are those of Stanczuk et al. (2022), and Horvat & Pfister (2024). The latter modifies the training procedure of DMs, so we focus on the former since we see compatibility with existing pre-trained models as an important requirement for DM-based LID estimators. Stanczuk et al. consider *variance-exploding* DMs, where $f = 0$. They show that, as $t \searrow 0$, the score function $s(x, t)$ points orthogonally towards the manifold containing x, or formally, it lies in the normal space of this manifold at x. They thus propose the following estimator, which we refer to as the normal bundle (NB) estimator: first run Equation 1 until time t_0 starting from x, and evaluate $\hat{s}(\cdot, t_0)$ at the resulting value; then repeat this process K times and stack the K resulting D-dimensional vectors into a matrix $S(x) \in \mathbb{R}^{D \times K}$. If t_0 is small enough and K is large enough, the columns of $S(x)$ span the normal space of the manifold at x, suggesting that the rank of this matrix estimates the dimension of this normal space, namely $D - \mathrm{LID}(x)$. Finally, they estimate $\mathrm{LID}(x)$ as:

$$\mathrm{LID}(x) \approx D - \operatorname{rank} S(x). \tag{9}$$

Although this estimator addresses some of the limitations of LIDL, it remains computationally expensive – computing $S(x)$ requires K function evaluations with the authors recommending $K = 4D$ – and as we will see later, it does not always produce reliable estimates.

3. Method

Although LIDL only used normalizing flows, the authors did point out that these models could be swapped for any other generative model admitting density evaluation. Indeed, one could trivially train m DMs and replace the flows with them. Throughout this section we assume access to a pre-trained DM such that $f(x, t) = b(t)x$ for a function $b : [0, 1] \to \mathbb{R}$. This choice implies that the transition kernel $p_{t|0}$ associated with Equation 1 is Gaussian (Särkkä & Solin, 2019):

$$p_{t|0}(x_t \mid x_0) = \mathcal{N}(x_t; \psi(t)x_0, \sigma^2(t)I_D), \tag{10}$$

where $\psi, \sigma : [0, 1] \to \mathbb{R}$. We also assume that b and g are such that ψ and σ are differentiable and such that $\lambda(t) \coloneqq \sigma(t)/\psi(t)$ is injective. This setting encompasses all DMs commonly used in practice, including variance-exploding, variance-preserving (of which DDPM (Ho et al., 2020) is a discretized instance), and sub-variance-preserving (Song et al., 2021b). In Appendix A we include explicit formulas for $\psi(t)$, $\sigma^2(t)$, and $\lambda(t)$ for these particular DMs.

3.1. LIDL with Diffusion Models

DMs operate by adding Gaussian noise to data and admit density evaluation of the resulting noisy distributions (Equation 5). This is precisely what LIDL requires, so for a given x and δ, we would like to relate $\varrho(x, \delta)$ to the density of the DM. In the case of variance-exploding DMs, $\psi(t) = 1$, in which case it is straightforward to see that $\varrho(x, \delta) = p(x, \sigma^{-1}(e^{\delta}))$.[3] In turn, we can use LIDL with a single variance-exploding DM by evaluating each $\hat{p}(x, \sigma^{-1}(e^{\delta_i}))$ through Equation 5. This idea extends beyond variance-exploding DMs; in Appendix C.1 we show that for any arbitrary DM with transition kernel as in Equation 10, it holds that

$$\log \varrho(x, \delta) = D \log \gamma(\delta) + \log p\big(\gamma(\delta)x, t(\delta)\big), \tag{11}$$

where $t(\delta) := \lambda^{-1}(e^{\delta})$ and $\gamma(\delta) := \psi(t(\delta))$, thus showing that LIDL can be used with a single DM.

3.2. An Efficient Implementation of LIDL with Diffusion Models

Using Equation 11 with LIDL involves computing $\log \hat{p}\big(\gamma(\delta_i)x, t(\delta_i)\big)$ through Equation 5, for each $i = 1, \dots, m$, before running the regression. Since each of the corresponding ODEs in Equation 4 starts at a different time $t_0 = t(\delta_i)$ and is evaluated at a different point $\gamma(\delta_i)x$, this means that a different ODE solver call would have to be used for each i, resulting in a prohibitively expensive procedure. By leveraging the Fokker-Planck equation associated with Equation 1, we show in Appendix C.2 that, for DMs with transition kernel as in Equation 10:

$$\frac{\partial}{\partial \delta} \log \varrho(x, \delta) = \sigma^2\big(t(\delta)\big) \Big(\operatorname{tr}\Big(\nabla s\big(\gamma(\delta)x, t(\delta)\big)\Big) + \big\|s\big(\gamma(\delta)x, t(\delta)\big)\big\|_2^2\Big) =: \nu\big(t(\delta); s, x\big). \tag{12}$$

Assuming without loss of generality that $\delta_1 < \dots < \delta_m$, solving the ODE

$$\mathrm{d} \log \hat{\varrho}(x, \delta) = \nu\big(t(\delta); \hat{s}, x\big)\mathrm{d}\delta, \quad \log \hat{\varrho}(x, \delta_1) = 0 \tag{13}$$

from δ_1 to δ_m produces the trajectory $(\log \hat{\varrho}(x, \delta))_{\delta \in [\delta_1, \delta_m]}$. Since $\nu(t(\delta); \hat{s}, x)$ does not depend on $\hat{\varrho}(x, \delta)$, if $\hat{s} = s$, then the solution will be such that $\log \hat{\varrho}(x, \delta) = \log \varrho(x, \delta) + c_{\text{init}}$ for some constant c_{init} that depends on the initial condition but not on δ. Thus, while setting the initial condition to 0 might at first appear odd, we can fit a regression as in LIDL, using $\{(\delta_i, \log \hat{\varrho}(x, \delta_i))\}_{i=1}^m$, and c_{init} will be absorbed in the intercept without affecting the slope. In other words, the initial condition is irrelevant, and we can use LIDL with DMs by calling a single ODE solver on Equation 13.

[3]Note that we treat positive and negative superindices differently: e.g. σ^{-1} denotes the inverse function of σ, not $1/\sigma$; on the other hand σ^2 denotes the square of σ, not $\sigma \circ \sigma$.

3.3. FLIPD: A Fokker-Planck-Based LID Estimator

The LIDL estimator with DMs presented in Section 3.2 provides a massive speedup over the naïve approach of training m DMs and over the method from Section 3.1 requiring m ODE solves. Yet, solving Equation 13 involves computing the trace of the Jacobian of $\hat{s}$ multiple times within an ODE solver, which, as mentioned in Section 2.1, remains expensive. In this section we present our LID estimator, FLIPD, which circumvents the need for an ODE solver altogether. Recall that LIDL is based on Equation 8, which justifies the regression. Differentiating this equation yields that $\partial/\partial\delta \log \varrho(x, \delta_0) \approx \text{LID}(x) - D$ for negative enough δ_0, meaning that Equation 12 directly provides the rate of change that the regression in LIDL aims to estimate, from which we get:

$$\text{LID}(x) \approx D + \frac{\partial}{\partial \delta} \log \varrho(x, \delta_0) \approx D + \nu\big(t(\delta_0); \hat{s}, x\big) =: \text{FLIPD}(x, t_0), \tag{14}$$

where $t_0 := t(\delta_0)$. In addition to not requiring an ODE solver, computing FLIPD requires only a single hyperparameter, whereas regression-based estimators require m. Since $\nu(t(\delta); \hat{s}, x)$ depends on δ only through $t(\delta)$, we can directly set t_0 as the hyperparameter rather than δ_0, which avoids the potentially cumbersome computation of $t(\delta_0) = \lambda^{-1}(e^{\delta_0})$: instead of setting a suitably negative δ_0, we set $t_0 > 0$ sufficiently close to 0. In Appendix A we include explicit formulas for $\text{FLIPD}(x, t_0)$ for common DMs.

Finally, we present a theoretical result further justifying FLIPD. Note that the $\mathcal{O}(1)$ term in Equation 7 need not be constant in δ as in Equation 8, even if it is bounded. The more this term deviates from a constant, the more bias we should expect in both LIDL and FLIPD. The following result shows that in an idealized linear setting, FLIPD is unaffected by this problem:

Theorem 3.1. *Let $\mathcal{L}$ be an embedded submanifold of $\mathbb{R}^D$ given by a d-dimensional affine subspace. If $p(\cdot, 0)$ is supported on $\mathcal{L}$, continuous, and with finite second moments, then for any $x \in \mathcal{L}$ with $p(x, 0) > 0$, we have:*

$$\lim_{\delta \to -\infty} \frac{\partial}{\partial \delta} \log \varrho(x, \delta) = d - D. \tag{15}$$

Proof. See Appendix C.3. □

We hypothesize that this result can be extended to non-linear submanifolds since, intuitively, every manifold can be locally linearly approximated (by its tangent space) and $\varrho(x, \delta)$ is "local as $\delta \to -\infty$" in the sense that its dependence on the values $p(y, 0)$ becomes negligible as $\delta \to -\infty$ (because $\mathcal{N}(0, e^{2\delta} I_D)$ approaches a point mass at 0) when y is not in a close enough neighbourhood of x. However, we leave generalizing our result to future work.

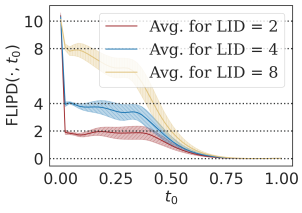

(a) Mixture of Gaussians.

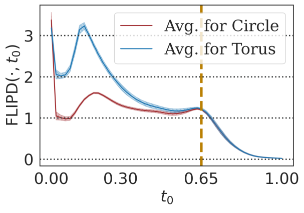

(b) String within a doughnut.

Figure 2: FLIPD curves with knees at the true LID.

4. Experiments

Throughout our experiments, we use variance-preserving DMs, the most popular variant of DMs, and compatible with DDPMs; see Appendix D.1 for the hyperparameter setup. We also include a "dictionary" to translate between the score-based formulation under which we developed FLIPD, and DDPMs, in Appendix B. Our code is written in PyTorch (Paszke et al., 2019), is available at `https://anonymous.4open.science/r/dgm-geometry-5D48/README.md`, and will be released upon publication.

The effect of t_0 FLIPD requires setting t_0 close to 0 (since all the theory holds in the $\delta \to -\infty$ regime). It is important to note that DMs fitted to low-dimensional manifolds are known to exhibit numerically unstable scores $s(\cdot, t_0)$ as $t_0 \searrow 0$ (Vahdat et al., 2021; Lu et al., 2023; Loaiza-Ganem et al., 2024). Our first set of experiments examines the effect of t_0 on $\text{FLIPD}(x, t_0)$ by varying t_0 within the range $(0, 1)$.

In Figure 2, we train DMs on two distributions: (i) a mixture of three isotropic Gaussians with dimensions 2, 4, and 8, embedded in $\mathbb{R}^{10}$ (each embedding is carried out by multiplication against a random matrix with orthonormal columns plus a random translation); and (ii) a "string within a doughnut", which is a mixture of uniform distributions on a 2d torus (with a major radius of 10 and a minor radius of 1) and a 1d circle (aligning with the major circle of the torus) embedded in $\mathbb{R}^3$ (this union of manifolds is shown in the upper half of Figure 3). While $\text{FLIPD}(x, t_0)$ is inaccurate at $t_0 = 0$ due to the aforementioned instabilities, it quickly stabilizes around the true LID for all datapoints. We refer to this pattern as a *knee* in the FLIPD curve. In Appendix D.2, we show similar curves for more complex data manifolds.

FLIPD is a multiscale estimator Interestingly, in Figure 2b we see that the blue FLIPD curve (corresponding to "doughnut" points with LID of 2) exhibits a second knee at 1, illustrated at the t_0 with a vertical line. This confirms the multiscale nature of convolution-based estimators, first postulated by Tempczyk et al. (2022) in the context of normalizing flows; they claim that when selecting a log standard deviation δ, all directions along which a datum

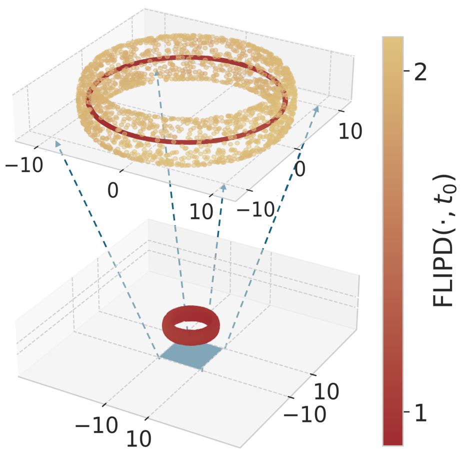

Figure 3: "String within a doughnut" manifolds, and corresponding FLIPD estimates for different values of t_0 ($t_0 = 0.05$ on top and $t_0 = 0.65$ on bottom). These results highlight the multiscale nature of FLIPD.

can vary with log standard deviation less than δ are ignored. The second knee in Figure 2b can be explained similarly: the torus looks like a 1d circle when viewed from far away, and larger values of t_0 correspond to viewing the manifolds from farther away. This is visualized in Figure 3 with two views of the "string within a doughnut" and corresponding LID estimates: one zoomed-in view where t_0 is small, providing fine-grained LID estimates, and a zoomed-out view of a 1d circle from this distance. In Appendix D.3 we have an experiment to make the multiscale argument explicit.

Finding knees As mentioned, we persistently see knees in FLIPD curves. Not only is this in line with the observations of LIDL on normalizing flows (see Figure 5 of Tempczyk et al. (2022)), but it also gives us a fully automated approach to setting t_0. We leverage `kneedle` (Satopaa et al., 2011), a knee detection algorithm which aims to find points of maximum curvature. When computationally sensible, rather than fixing t_0, we evaluate Equation 14 for 50 values of t_0 and pass the results to `kneedle` to automatically detect the t_0 where a knee occurs.

Synthetic experiments We create a benchmark for LID evaluation on complex unions of manifolds where true LID is known. We sample from simple distributions on low-dimensional spaces, and then embed the samples into $\mathbb{R}^D$. We denote uniform, Gaussian, and Laplace distributions as $\mathcal{U}, \mathcal{N}$, and $\mathcal{L}$, respectively, with sub-indices indicating LID, and a plus sign denoting mixtures. To embed samples into higher dimensions, we apply a random matrix with orthonormal columns and then apply a random translation. For example, $\mathcal{N}_{10} + \mathcal{L}_{20} \subseteq \mathbb{R}^{100}$ indicates a 10-dimensional Gaussian and a 20-dimensional Laplace, each of which undergoes a random affine transformation mapping to $\mathbb{R}^{100}$

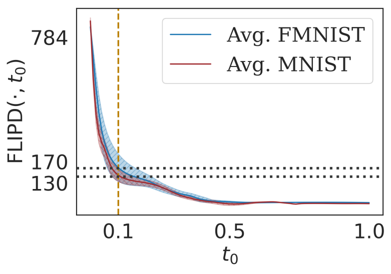

(a) FLIPD of MNIST and FMNIST.

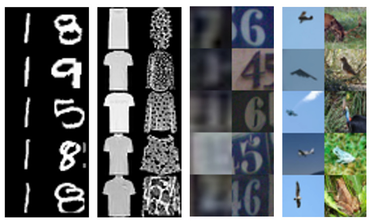

(b) Ordering small images.

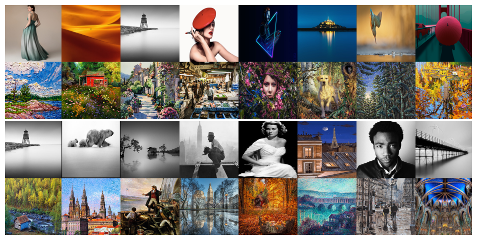

(c) Ordering high-resolution images in LAION using FLIPD (top) and PNG compression size (bottom).

Figure 4: Overview of image LID: **(a)** shows the FLIPD curves that are used to estimate average LID for MNIST and FMNIST; **(b)** compares images with small and large FLIPD estimates from FMNIST, MNIST, SVHN, and CIFAR10; and **(c)** compares Stable Diffusion images with small and large FLIPD estimates (top, $t_0 = 0.5$) and PNG compression sizes (bottom).

(one transformation per component). We also generate non-linear manifolds, denoted with $\mathcal{F}$, by applying a randomly initialized D-dimensional neural spline flow (Durkan et al., 2019) after the affine transformation (when using flows, the input noise is always uniform); since the flow is a diffeomorphism, it preserves LID. To our knowledge, this synthetic LID benchmark is the most extensive to date, revealing surprising deficiencies in some well-known traditional estimators. For an in-depth analysis, see Appendix D.4.

Here, we summarize our synthetic experiments in Table 1 using two metrics of performance: the mean absolute error (MAE) between the predicted and true LID for individual datapoints; and the concordance index, which measures similarity in the rankings between then true LIDs and the estimated ones (note that this metric only makes sense when the dataset has variability in its ground truth LIDs, so we only report it for the appropriate entries in Table 1). We compare against the NB and LIDL estimators described in Section 2.2, as well as two of the most performant model-free baselines: LPCA (Fukunaga & Olsen, 1971; Cangelosi & Goriely, 2007) and ESS (Johnsson et al., 2014). For the NB baseline, we use the exact same DM backbone as for FLIPD (since NB was designed for variance-exploding DMs, we use the adaptation to variance-preserving DMs used by Kamkari et al. (2024b), which produces extremely similar results), and for LIDL we use 8 neural spline flows. In terms of MAE, we find that FLIPD tends to be the best model-based estimator, particularly as dimension increases. Although model-free baselines perform well in simplistic scenarios, they produce unreliable results as LID increases or more non-linearity is introduced in the data manifold. In terms of concordance index, FLIPD achieves *perfect* scores in all scenarios, meaning that even when its estimates are off, it always provides correct LID rankings. We include additional results in the appendices: in Appendix D.5 we ablate FLIPD, finding that using `kneedle` indeed helps, and that FLIPD also outperforms the efficient implementation of LIDL with DMs described in Section 3.2. We notice that NB with the setting proposed in Stanczuk et al. (2022) consistently produces estimates that are almost equal to the ambient dimension; thus, in Appendix D.6 we also show how NB can be significantly improved upon by using `kneedle`, although it is still outperformed by FLIPD. In Appendix D.4 we include comparisons on more high-dimensional datasets, and also compare against other model-free baselines such as MLE (Levina & Bickel, 2004; MacKay & Ghahramani, 2005) and FIS (Albergante et al., 2019).

Image experiments We first focus on the simple image datasets MNIST (LeCun et al., 1998) and FMNIST (Xiao et al., 2017). We flatten the images and use the same MLP architecture as in our synthetic experiments. Despite using an MLP, our DMs can generate reasonable samples (Appendix E.1) and the FLIPD curve for both MNIST and FMNIST is shown in Figure 4a. The knee points are identified at $t_0 = 0.1$, resulting in average LID estimates of approximately 130 and 170, respectively. Evaluating LID estimates for image data is challenging due to the lack of ground truth. Although our LID estimates are higher than those obtained by Pope et al. (2021) and Brown et al. (2023), our high-dimensional experiments (Table 7 of Appendix D.4) and findings by Tempczyk et al. (2022) and Stanczuk et al. (2022) show that model-free baselines underestimate LID of high-dimensional data, especially images.

When moving to more complex image datasets, the simplistic MLP score network backbone fails to generate high-quality samples. Therefore, we replace it with state-of-the-art UNets (Ronneberger et al., 2015; von Platen et al., 2022) (see Appendix E.2). As long as the DM accurately fits the data manifold, our theory should hold, regardless of the choice of backbone. Yet, we see that UNets do not produce a clear knee in the FLIPD curves (see curves in Figure 10 of Appendix E.1). We discuss why this might be the case in Appendix E.1, and from here on we simply set t_0 as a hyperparameter instead of using `kneedle`. Despite FLIPD curves lacking a knee when using UNets, we argue that our estimates remain valuable measures of complexity. We took a random subset of 4096 images from

Table 1: MAE (lower is better) | concordance indices (higher is better with 1.0 being the gold standard). Rows show synthetic manifolds and columns represent LID estimation methods. Columns are grouped based on whether they use a generative model, with the best results for each metric within each group being bolded.

	Model-based			Model-free	
Synthetic Manifold	FLIPD	NB	LIDL	ESS	LPCA
String within doughnut $\subseteq \mathbb{R}^3$	**0.06** | **1.00**	1.48 | 0.48	1.10 | 0.99	0.02 | **1.00**	**0.00** | **1.00**
$\mathcal{L}_5 \subseteq \mathbb{R}^{10}$	0.17 | –	1.00 | –	**0.10** | –	0.07 | –	**0.00** | –
$\mathcal{N}_{90} \subseteq \mathbb{R}^{100}$	0.49 | –	**0.18** | –	0.33 | –	**1.67** | –	21.9 | –
$\mathcal{U}_{10} + \mathcal{U}_{30} + \mathcal{U}_{90} \subseteq \mathbb{R}^{100}$	**1.30** | **1.00**	61.6 | 0.34	8.46 | 0.74	21.9 | 0.74	**20.1** | **0.86**
$\mathcal{N}_{10} + \mathcal{N}_{25} + \mathcal{N}_{50} \subseteq \mathbb{R}^{100}$	**1.81** | **1.00**	74.2 | 0.34	8.87 | 0.74	7.71 | 0.88	**5.72** | **0.91**
$\mathcal{F}_{10} + \mathcal{F}_{25} + \mathcal{F}_{50} \subseteq \mathbb{R}^{100}$	**3.93** | **1.00**	74.2 | 0.34	18.6 | 0.70	9.20 | 0.90	**6.77** | **1.00**
$\mathcal{U}_{10} + \mathcal{U}_{80} + \mathcal{U}_{200} \subseteq \mathbb{R}^{800}$	**14.3** | **1.00**	715 | 0.34	120 | 0.70	**2.35** | **1.00**	33.7 | **1.00**
$\mathcal{U}_{900} \subseteq \mathbb{R}^{1000}$	**12.8** | –	100 | –	24.9 | –	**75.2** | –	801 | –

Table 2: Spearman's correlation between LID estimates and PNG compression size.

Method	MNIST	FMNIST	CIFAR10	SVHN
FLIPD	0.837	**0.883**	0.819	**0.876**
NB	**0.864**	0.480	**0.894**	0.573
ESS	0.444	0.063	0.326	0.019
LPCA	0.413	0.01	0.302	-0.008

FMNIST, MNIST, CIFAR10 (Krizhevsky & Hinton, 2009), and SVHN (Netzer et al., 2011), and sorted them according to their FLIPD estimates. We show the top and bottom 5 images for each dataset in Figure 4b, and include more samples in Appendix E.3. Our visualization shows that higher FLIPD estimates indeed correspond to images with more detail and texture, while lower estimates correspond to less complex ones. Additionally, we show in Appendix E.4 that using only 50 Hutchinson samples to approximate the trace term in FLIPD is sufficient for small values of t_0: FLIPD not only visually corresponds to image complexity, but also required only 50 Jacobian-vector-products, resulting in a significant speedup over all prior work.

Further, we quantitatively assess our estimates by computing Spearman's rank correlation coefficient between different LID estimators and PNG compression size, used as a proxy for complexity in the absence of ground truth. As shown in Table 2, FLIPD has a high correlation with PNG, whereas model-free estimators do not. We find that the NB estimator correlates slightly more with PNG on MNIST and CIFAR10, but significantly less in FMNIST and SVHN. We also highlight that NB requires $\sim$ 3000 function evaluations to produce a single LID estimate for MNIST and FMNIST, and $\sim$ 12000 for SVHN and CIFAR10 – a massive increase in computation as compared to the 50 Jacobian-vector-products we used for FLIPD.

Finally, we consider high-resolution images from LAION aesthetics (Schuhmann et al., 2022) and, for the first time, estimate LID for extremely high-dimensional images with $D = 3 \times 512 \times 512 = 786432$. To achieve this, we use Stable Diffusion (Rombach et al., 2022), a latent DM pretrained on LAION-5B (Schuhmann et al., 2022). This includes an encoder and a decoder trained to preserve relevant characteristics of the data manifold in latent representations. Since the encoder and decoder are continuous and effectively invert each other, we argue that the Stable Diffusion encoder can, for practical purposes, be considered a topological embedding of the LAION-5B dataset into its latent space of dimension $4 \times 64 \times 64 = 16384$. Therefore, the dimension of the LAION-5B submanifold in latent space should be unchanged. This approximation allows us to estimate image LIDs by carrying out FLIPD in the latent space of Stable Diffusion. Here, we set the Hutchinson sample count to 1, meaning we only require a *single* Jacobian-vector-product. When we order a random subset of 1600 samples according to their FLIPD at $t_0 = 0.3$, the more complex images are clustered at the end, while the least complex are clustered at the beginning: see Figure 1 and Figure 4c for the lowest- and highest-LID images from this ordering, and Figure 25 in Appendix E.6 to view the entire subset and other values of t_0. In comparison to orderings according to PNG compression size (Figure 4c), FLIPD estimates prioritize semantic complexity over low-level details like colouration.

5. Conclusions, Limitations, and Future Work

In this work, we have shown that the Fokker-Planck equation can be utilized for efficient LID estimation with any pre-trained DM. We have provided strong theoretical foundations and extensive benchmarks showing that FLIPD estimates accurately reflect data complexity. Although FLIPD produces excellent LID estimates on synthetic benchmarks, the lack of knees in FLIPD curves on image data when using state-of-the-art architectures is surprising, and results in unstable LID estimates which strongly depend on t_0. We see this behaviour as a limitation, even if FLIPD provides a meaningful measure of complexity in these cases. Given that FLIPD is tractable, differentiable, and compatible with any DM, we hope that it will find uses in applications where LID estimates have already proven helpful, including OOD detection, AI-generated data analysis, and adversarial example detection.

References

Albergante, L., Bac, J., and Zinovyev, A. Estimating the effective dimension of large biological datasets using fisher separability analysis. In *2019 International Joint Conference on Neural Networks*, pp. 1–8. IEEE, 2019.

Anderberg, A., Bailey, J., Campello, R. J., Houle, M. E., Marques, H. O., Radovanović, M., and Zimek, A. Dimensionality-aware outlier detection. In *Proceedings of the 2024 SIAM International Conference on Data Mining*, pp. 652–660, 2024.

Anderson, B. D. Reverse-time diffusion equation models. *Stochastic Processes and their Applications*, 12(3):313–326, 1982.

Ansuini, A., Laio, A., Macke, J. H., and Zoccolan, D. Intrinsic dimension of data representations in deep neural networks. In *Advances in Neural Information Processing Systems*, 2019.

Bac, J., Mirkes, E. M., Gorban, A. N., Tyukin, I., and Zinovyev, A. Scikit-Dimension: A Python Package for Intrinsic Dimension Estimation. *Entropy*, 23(10):1368, 2021.

Baydin, A. G., Pearlmutter, B. A., Radul, A. A., and Siskind, J. M. Automatic Differentiation in Machine Learning: A Survey. *Journal of Machine Learning Research*, 18:1–43, 2018.

Bengio, Y., Courville, A., and Vincent, P. Representation learning: A review and new perspectives. *IEEE Transactions on Pattern Analysis and Machine Intelligence*, 35 (8):1798–1828, 2013.

Birdal, T., Lou, A., Guibas, L. J., and Simsekli, U. Intrinsic dimension, persistent homology and generalization in neural networks. In *Advances in Neural Information Processing Systems*, 2021.

Brown, B. C., Juravsky, J., Caterini, A. L., and Loaiza-Ganem, G. Relating regularization and generalization through the intrinsic dimension of activations. *arXiv:2211.13239*, 2022.

Brown, B. C., Caterini, A. L., Ross, B. L., Cresswell, J. C., and Loaiza-Ganem, G. Verifying the union of manifolds hypothesis for image data. In *International Conference on Learning Representations*, 2023.

Cangelosi, R. and Goriely, A. Component retention in principal component analysis with application to cdna microarray data. *Biology Direct*, 2:1–21, 2007.

Chen, R. T., Rubanova, Y., Bettencourt, J., and Duvenaud, D. K. Neural ordinary differential equations. In *Advances in Neural Information Processing Systems*, 2018.

Cornish, R., Caterini, A. L., Deligiannidis, G., and Doucet, A. Relaxing bijectivity constraints with continuously indexed normalising flows. In *International Conference on Machine Learning*, pp. 2133–2143, 2020.

Cresswell, J. C., Ross, B. L., Loaiza-Ganem, G., Reyes-Gonzalez, H., Letizia, M., and Caterini, A. L. CaloMan: Fast generation of calorimeter showers with density estimation on learned manifolds. *arXiv:2211.15380*, 2022.

De Bortoli, V. Convergence of denoising diffusion models under the manifold hypothesis. *Transactions on Machine Learning Research*, 2022.

Dinh, L., Sohl-Dickstein, J., and Bengio, S. Density estimation using Real NVP. In *International Conference on Learning Representations*, 2017.

Durkan, C., Bekasov, A., Murray, I., and Papamakarios, G. Neural spline flows. In *Advances in Neural Information Processing Systems*, 2019.

Durkan, C., Bekasov, A., Murray, I., and Papamakarios, G. nflows: normalizing flows in PyTorch, November 2020. URL https://doi.org/10.5281/zenodo.4296287.

Facco, E., d'Errico, M., Rodriguez, A., and Laio, A. Estimating the intrinsic dimension of datasets by a minimal neighborhood information. *Scientific Reports*, 7(1): 12140, 2017.

Falconer, K. *Fractal Geometry: Mathematical Foundations and Applications*. John Wiley & Sons, 2007.

Fukunaga, K. and Olsen, D. R. An algorithm for finding intrinsic dimensionality of data. *IEEE Transactions on Computers*, 100(2):176–183, 1971.

Harrell Jr, F. E., Lee, K. L., and Mark, D. B. Multivariable prognostic models: issues in developing models, evaluating assumptions and adequacy, and measuring and reducing errors. *Statistics in Medicine*, 15(4):361–387, 1996.

Haussmann, U. and Pardoux, E. Time reversal of diffusions. *The Annals of Probability*, 14(4):1188–1205, 1986.

Ho, J., Jain, A., and Abbeel, P. Denoising diffusion probabilistic models. In *Advances in Neural Information Processing Systems*, 2020.

Horvat, C. and Pfister, J.-P. On gauge freedom, conservativity and intrinsic dimensionality estimation in diffusion models. In *International Conference on Learning Representations*, 2024.

Houle, M. E., Schubert, E., and Zimek, A. On the correlation between local intrinsic dimensionality and outlierness. In *Similarity Search and Applications: 11th International Conference, SISAP 2018*, pp. 177–191. Springer, 2018.

Hurewicz, W. and Wallman, H. *Dimension Theory (PMS-4)*. Princeton University Press, 1948.

Hutchinson, M. F. A stochastic estimator of the trace of the influence matrix for Laplacian smoothing splines. *Communications in Statistics-Simulation and Computation*, 18(3):1059–1076, 1989.

Johnsson, K., Soneson, C., and Fontes, M. Low bias local intrinsic dimension estimation from expected simplex skewness. *IEEE Transactions on Pattern Analysis and Machine Intelligence*, 37(1):196–202, 2014.

Kamkari, H., Balazadeh, V., Zehtab, V., and Krishnan, R. G. Order-based structure learning with normalizing flows. *arXiv:2308.07480*, 2024a.

Kamkari, H., Ross, B. L., Cresswell, J. C., Caterini, A. L., Krishnan, R. G., and Loaiza-Ganem, G. A geometric explanation of the likelihood OOD detection paradox. *arXiv:2403.18910*, 2024b.

Kingma, D. P. and Welling, M. Auto-encoding variational Bayes. In *International Conference on Learning Representations*, 2014.

Kirichenko, P., Izmailov, P., and Wilson, A. G. Why normalizing flows fail to detect out-of-distribution data. In *Advances in Neural Information Processing Systems*, 2020.

Krizhevsky, A. and Hinton, G. Learning multiple layers of features from tiny images. *Technical Report*, 2009.

LeCun, Y., Bottou, L., Bengio, Y., and Haffner, P. Gradient-based learning applied to document recognition. *Proceedings of the IEEE*, 86(11):2278–2324, 1998.

Lee, J. M. *Introduction to Smooth Manifolds*. Springer, 2nd edition, 2012.

Levina, E. and Bickel, P. Maximum likelihood estimation of intrinsic dimension. In *Advances in Neural Information Processing Systems*, 2004.

Loaiza-Ganem, G., Ross, B. L., Cresswell, J. C., and Caterini, A. L. Diagnosing and fixing manifold overfitting in deep generative models. *Transactions on Machine Learning Research*, 2022.

Loaiza-Ganem, G., Ross, B. L., Hosseinzadeh, R., Caterini, A. L., and Cresswell, J. C. Deep generative models through the lens of the manifold hypothesis: A survey and new connections. *arXiv:2404.02954*, 2024.

Lu, Y., Wang, Z., and Bal, G. Mathematical analysis of singularities in the diffusion model under the submanifold assumption. *arXiv:2301.07882*, 2023.

Ma, X., Li, B., Wang, Y., Erfani, S. M., Wijewickrema, S., Schoenebeck, G., Song, D., Houle, M. E., and Bailey, J. Characterizing adversarial subspaces using local intrinsic dimensionality. In *International Conference on Learning Representations*, 2018.

MacKay, D. J. and Ghahramani, Z. Comments on "Maximum likelihood estimation of intrinsic dimension' by E. Levina and P. Bickel (2004). *The Inference Group Website, Cavendish Laboratory, Cambridge University*, 2005.

Magai, G. and Ayzenberg, A. Topology and geometry of data manifold in deep learning. *arXiv:2204.08624*, 2022.

Mayr, P. and Petras, V. Cross-concordances: terminology mapping and its effectiveness for information retrieval. *arXiv:0806.3765*, 2008.

Netzer, Y., Wang, T., Coates, A., Bissacco, A., Wu, B., and Ng, A. Y. Reading digits in natural images with unsupervised feature learning. In *NIPS Workshop on Deep Learning and Unsupervised Feature Learning*, 2011.

Paszke, A., Gross, S., Massa, F., Lerer, A., Bradbury, J., Chanan, G., Killeen, T., Lin, Z., Gimelshein, N., Antiga, L., et al. Pytorch: An imperative style, high-performance deep learning library. In *Advances in Neural Information Processing Systems*, 2019.

Pidstrigach, J. Score-based generative models detect manifolds. In *Advances in Neural Information Processing Systems*, 2022.

Pope, P., Zhu, C., Abdelkader, A., Goldblum, M., and Goldstein, T. The intrinsic dimension of images and its impact on learning. In *International Conference on Learning Representations*, 2021.

Rezende, D. and Mohamed, S. Variational Inference with Normalizing Flows. In *Proceedings of the 32nd International Conference on Machine Learning*, volume 37, pp. 1530–1538, 2015.

Rombach, R., Blattmann, A., Lorenz, D., Esser, P., and Ommer, B. High-resolution image synthesis with latent diffusion models. In *Proceedings of the IEEE/CVF Conference on Computer Vision and Pattern Recognition*, pp. 10684–10695, 2022.

Ronneberger, O., Fischer, P., and Brox, T. U-net: Convolutional networks for biomedical image segmentation. In *Medical image computing and computer-assisted* *intervention–MICCAI 2015: 18th international conference, Munich, Germany, October 5-9, 2015, proceedings, part III 18*, pp. 234–241. Springer, 2015.

Särkkä, S. and Solin, A. *Applied stochastic differential equations*. Cambridge University Press, 2019.

Satopaa, V., Albrecht, J., Irwin, D., and Raghavan, B. Finding a "kneedle" in a Haystack: Detecting Knee Points in System Behavior. In *31st International Conference on Distributed Computing Systems Workshops*, pp. 166–171. IEEE, 2011.

Schuhmann, C., Beaumont, R., Vencu, R., Gordon, C., Wightman, R., Cherti, M., Coombes, T., Katta, A., Mullis, C., Wortsman, M., et al. Laion-5b: An open large-scale dataset for training next generation image-text models. *Advances in Neural Information Processing Systems*, 35: 25278–25294, 2022.

Sohl-Dickstein, J., Weiss, E., Maheswaranathan, N., and Ganguli, S. Deep unsupervised learning using nonequilibrium thermodynamics. In *International Conference on Machine Learning*, pp. 2256–2265, 2015.

Song, Y., Durkan, C., Murray, I., and Ermon, S. Maximum likelihood training of score-based diffusion models. In *Advances in Neural Information Processing Systems*, 2021a.

Song, Y., Sohl-Dickstein, J., Kingma, D. P., Kumar, A., Ermon, S., and Poole, B. Score-based generative modeling through stochastic differential equations. In *International Conference on Learning Representations*, 2021b.

Stanczuk, J., Batzolis, G., Deveney, T., and Schönlieb, C.-B. Your diffusion model secretly knows the dimension of the data manifold. *arXiv:2212.12611*, 2022.

Steck, H., Krishnapuram, B., Dehing-Oberije, C., Lambin, P., and Raykar, V. C. On ranking in survival analysis: Bounds on the concordance index. In *Advances in Neural Information Processing Systems*, volume 20, 2007.

Teles, J. Concordance coefficients to measure the agreement among several sets of ranks. *Journal of Applied Statistics*, 39(8):1749–1764, 2012.

Tempczyk, P., Michaluk, R., Garncarek, L., Spurek, P., Tabor, J., and Golinski, A. LIDL: Local intrinsic dimension estimation using approximate likelihood. In *International Conference on Machine Learning*, pp. 21205–21231, 2022.

Tulchinskii, E., Kuznetsov, K., Kushnareva, L., Cherniavskii, D., Nikolenko, S., Burnaev, E., Barannikov, S., and Piontkovskaya, I. Intrinsic dimension estimation for robust detection of ai-generated texts. In *Advances in Neural Information Processing Systems*, 2023.

Vahdat, A., Kreis, K., and Kautz, J. Score-based generative modeling in latent space. In *Advances in Neural Information Processing Systems*, 2021.

Valeriani, L., Doimo, D., Cuturello, F., Laio, A., Ansuini, A., and Cazzaniga, A. The geometry of hidden representations of large transformer models. In *Advances in Neural Information Processing Systems*, 2023.

Vincent, P. A connection between score matching and denoising autoencoders. *Neural Computation*, 23(7):1661–1674, 2011.

von Platen, P., Patil, S., Lozhkov, A., Cuenca, P., Lambert, N., Rasul, K., Davaadorj, M., and Wolf, T. Diffusers: State-of-the-art diffusion models. `https://github.com/huggingface/diffusers`, 2022.

Xiao, H., Rasul, K., and Vollgraf, R. Fashion-MNIST: A novel image dataset for benchmarking machine learning algorithms. *arXiv:1708.07747*, 2017.

Xue, F., Yang, B., Qi, Y., and Xin, J. Searching intrinsic dimensions of vision transformers. *arXiv:2204.07722*, 2022.

Zheng, Y., He, T., Qiu, Y., and Wipf, D. P. Learning manifold dimensions with conditional variational autoencoders. In *Advances in Neural Information Processing Systems*, 2022.

Zhu, W., Qiu, Q., Huang, J., Calderbank, R., Sapiro, G., and Daubechies, I. Ldmnet: Low dimensional manifold regularized neural networks. In *Proceedings of the IEEE Conference on Computer Vision and Pattern Recognition*, pp. 2743–2751, 2018.

A. Explicit Formulas

A.1. Variance-Exploding Diffusion Models

Variance-exploding DMs are such that $f(x,t) = 0$ with g being non-zero. In this case (Song et al., 2021b):

$$\psi(t) = 1, \quad \text{and} \quad \sigma^2(t) = \int_0^t g^2(u)\mathrm{d}u. \tag{16}$$

Since g is non-zero, g^2 is positive, so that σ^2 is increasing, and thus injective. It follows that σ is also injective, so that $\lambda = \sigma/\psi = \sigma$ is injective. Equation 14 then implies that

$$\mathrm{FLIPD}(x, t_0) = D + \sigma^2(t_0)\left[\mathrm{tr}\left(\nabla s(x,t_0)\right) + \|s(x,t_0)\|_2^2\right]. \tag{17}$$

A.2. Variance-Preserving Diffusion Models (DDPMs)

Variance-preserving DMs are such that

$$f(x,t) = -\frac{1}{2}\beta(t)x, \quad \text{and} \quad g(t) = \sqrt{\beta(t)}, \tag{18}$$

where β is a positive scalar function. In this case (Song et al., 2021b):

$$\psi(t) = e^{-\frac{1}{2}B(t)}, \quad \text{and} \quad \sigma^2(t) = 1 - e^{-B(t)}, \quad \text{where} \quad B(t) \coloneqq \int_0^t \beta(u)\mathrm{d}u. \tag{19}$$

We then have that

$$\lambda(t) = \sqrt{\frac{\sigma^2(t)}{\psi^2(t)}} = \sqrt{e^{B(t)} - 1}. \tag{20}$$

Since β is positive, B is increasing and thus injective, from which it follows that λ is injective as well. Plugging everything into Equation 14, we obtain:

$$\mathrm{FLIPD}(x,t_0) = D + \left(1 - e^{-B(t_0)}\right)\left(\mathrm{tr}\left(\nabla s(e^{-\frac{1}{2}B(t_0)}x, t_0)\right) + \left\|s(e^{-\frac{1}{2}B(t_0)}x, t_0)\right\|_2^2\right). \tag{21}$$

A.3. Sub-Variance-Preserving Diffusion Models

Sub-variance-preserving DMs are such that

$$f(x,t) = -\frac{1}{2}\beta(t)x, \quad \text{and} \quad g(t) = \sqrt{\beta(t)\left(1 - e^{-2B(t)}\right)}, \quad \text{where} \quad B(t) \coloneqq \int_0^t \beta(u)\mathrm{d}u, \tag{22}$$

and where β is a positive scalar function. In this case (Song et al., 2021b):

$$\psi(t) = e^{-\frac{1}{2}B(t)}, \quad \text{and} \quad \sigma^2(t) = \left(1 - e^{-B(t)}\right)^2. \tag{23}$$

We then have that

$$\lambda(t) = \frac{\sigma(t)}{\psi(t)} = e^{\frac{1}{2}B(t)} - e^{-\frac{1}{2}B(t)} = 2\sinh\left(\frac{1}{2}B(t)\right). \tag{24}$$

Since β is positive, B is increasing and thus injective, from which it follows that λ is injective as well due to the injectivity of $\sinh$. Plugging everything into Equation 14, we obtain:

$$\mathrm{FLIPD}(x,t_0) = D + \left(1 - e^{-B(t_0)}\right)^2\left(\mathrm{tr}\left(\nabla s(e^{-\frac{1}{2}B(t_0)}x, t_0)\right) + \left\|s(e^{-\frac{1}{2}B(t_0)}x, t_0)\right\|_2^2\right). \tag{25}$$

Table 3: Comparing the discretized DDPM notation with score-based DM side-by-side.

Term	DDPM (Ho et al., 2020)	Score-based DM (Song et al., 2021b)
Timestep	$t \in \{0, 1, \dots, T\}$	$t/T = t \in [0, 1]$
(Noised out) datapoint	x_t	$x_{t/T} = x_t$
Diffusion process hyperparameter	β_t	$\beta(t/T) = \beta(t)$
Mean of transition kernel	$\sqrt{\bar{\alpha}_t}$	$\psi(t/T) = \psi(t)$
Std of transition kernel	$\sqrt{1 - \bar{\alpha}_t}$	$\sigma(t/T) = \sigma(t)$
Network parameterization	$-\epsilon(x, t)/\sqrt{1 - \bar{\alpha}_t}$	$\hat{s}(x, t/T) = \hat{s}(x, t)$

B. Adapting FLIPD for DDPMs

Here, we adapt FLIPD for state-of-the-art DDPM architectures and follow the discretized notation from Ho et al. (2020) where instead of using a continuous time index t from 0 to 1, a timestep t belongs instead to the sequence $\{0, \dots, T\}$ with T being the largest timescale. We use the colour gold to indicate the notation used by Ho et al. (2020). We highlight that the content of this section is a summary of the equivalence between DDPMs and the score-based formulation established by Song et al. (2021b).

As a reminder, DDPMs can be viewed as discretizations of the *forward* SDE process of a DM, where the process turns into a Markov *noising* process:

$$p(x_t \mid x_{t-1}) \coloneqq \mathcal{N}(x_t; \sqrt{1 - \beta_t} \cdot x_{t-1}, \beta_t I_D). \tag{26}$$

We also use sub-indices t instead of functions evaluated at t to keep consistent with Ho et al. (2020)'s notation. This in turn implies the following transition kernel:

$$p(x_t \mid x_0) = \mathcal{N}(x_t; \sqrt{\bar{\alpha}_t} x_0, (1 - \bar{\alpha}_t) I_D) \tag{27}$$

where $\alpha_t \coloneqq 1 - \beta_t$ and $\bar{\alpha}_t \coloneqq \prod_{s=1}^{t} \alpha_t$.

DDPMs model the *backward* diffusion process (or *denoising* process) by modelling a network $\epsilon : \mathbb{R}^D \times \{1, \dots, T\} \to \mathbb{R}^D$ that takes in a noised-out point and outputs a residual that can be used to denoise. In particular, for every t:

$$x_t + \epsilon(x_t, t) \sim p(x_{t-1} | x_t). \tag{28}$$

Song et al. (2021b) show that one can draw an equivalence between network $\epsilon(\cdot, t)$ and the score network (see their Appendix B). Here, we rephrase the connections in a more explicit manner where we note that:

$$-\epsilon(x, t)/\sqrt{1 - \bar{\alpha}_t} = s(x, t/T). \tag{29}$$

Consequently, plugging into Equation 21, we get the following formula adapted for DDPMs:

$$\text{FLIPD}(x, t_0) = D - \sqrt{1 - \bar{\alpha}_{t_0}} \operatorname{tr}\left(\nabla \epsilon(\sqrt{\bar{\alpha}_{t_0}} x, t_0)\right) + \|\epsilon(\sqrt{\bar{\alpha}_{t_0}} x, t_0)\|_2^2, \tag{30}$$

where $t_0 = t_0 \times T$ (best viewed in colour). We include Table 3, which summarizes all of the equivalent notation when moving from DDPMs to score-based DMs and vice-versa.

C. Proofs and Derivations

C.1. Derivation of Equation 11

We have that:

$$
\begin{aligned}
p\big(\gamma(\delta)x, t(\delta)\big) &= \int p_{t(\delta)|0}\big(\gamma(\delta)x \mid x_0\big)p(x_0, 0)\mathrm{d}x_0 && (31)\\
&= \int \mathcal{N}\Big(\gamma(\delta)x; \psi\big(t(\delta)\big)x_0, \sigma^2\big(t(\delta)\big)I_D\Big)p(x_0, 0)\mathrm{d}x_0 && (32)\\
&= \int \mathcal{N}\Big(\gamma(\delta)x; \gamma(\delta)x_0, \sigma^2\big(t(\delta)\big)I_D\Big)p(x_0, 0)\mathrm{d}x_0 && (33)\\
&= \frac{1}{\gamma^D(\delta)} \int \mathcal{N}\left(x; x_0, \frac{\sigma^2\big(t(\delta)\big)}{\psi^2\big(t(\delta)\big)}I_D\right) p(x_0, 0)\mathrm{d}x_0 && (34)\\
&= \frac{1}{\gamma^D(\delta)} \int \mathcal{N}\Big(x; x_0, \lambda^2\big(t(\delta)\big)I_D\Big)p(x_0, 0)\mathrm{d}x_0 && (35)\\
&= \frac{1}{\gamma^D(\delta)} \int \mathcal{N}\big(x; x_0, e^{2\delta}I_D\big)p(x_0, 0)\mathrm{d}x_0 = \frac{1}{\gamma^D(\delta)}\varrho(x, \delta), && (36)
\end{aligned}
$$

where we used that $\mathcal{N}(ax; ax_0, \sigma^2 I_D) = \frac{1}{a^D}\mathcal{N}(x; x_0, (\sigma^2/a^2)I_D)$. Taking logarithms yields Equation 11.

C.2. Derivation of Equation 12

First, we recall the Fokker-Planck equation associated with the SDE in Equation 1, which states that:

$$
\frac{\partial}{\partial t}p(x, t) = -p(x, t)\left[\nabla \cdot f(x, t)\right] - \langle f(x, t), \nabla p(x, t)\rangle + \frac{1}{2}g^2(t)\,\mathrm{tr}\left(\nabla^2 p(x, t)\right). \tag{37}
$$

We begin by using this equation to derive $\partial/\partial t \, \log p(x, t)$. Noting that $\nabla p(x, t) = p(x, t)s(x, t)$, we have that:

$$
\begin{aligned}
\mathrm{tr}\left(\nabla^2 p(x, t)\right) &= \mathrm{tr}\left(\nabla\left[p(x, t)s(x, t)\right]\right) = p(x, t)\,\mathrm{tr}\left(\nabla s(x, t)\right) + \mathrm{tr}\left(s(x, t)\nabla p(x, t)^\top\right) && (38)\\
&= p(x, t)\left[\mathrm{tr}\left(\nabla s(x, t)\right) + \|s(x, t)\|_2^2\right]. && (39)
\end{aligned}
$$

Because

$$
\frac{\partial}{\partial t}p(x, t) = p(x, t)\frac{\partial}{\partial t}\log p(x, t), \tag{40}
$$

it then follows that

$$
\frac{\partial}{\partial t}\log p(x, t) = -\left[\nabla \cdot f(x, t)\right] - \langle f(x, t), s(x, t)\rangle + \frac{1}{2}g^2(t)\left[\mathrm{tr}\left(\nabla s(x, t)\right) + \|s(x, t)\|_2^2\right]. \tag{41}
$$

Then, from Equation 11 and the chain rule, we get:

$$\frac{\partial}{\partial \delta} \log \varrho(x,\delta) = \frac{\mathrm{d}}{\mathrm{d}\delta}\left[D \log \psi\big(t(\delta)\big) + \log p\Big(\psi\big(t(\delta)\big)x, t(\delta)\Big)\right] \tag{42}$$

$$\begin{aligned} &= D\left[\frac{\mathrm{d}}{\mathrm{d}\delta}\log \psi\big(t(\delta)\big)\right] \\ &\quad + \begin{pmatrix} \nabla \log p\Big(\psi\big(t(\delta)\big)x, t(\delta)\Big) \\ \frac{\partial}{\partial t}\log p\Big(\psi\big(t(\delta)\big)x, t(\delta)\Big)\end{pmatrix}^{\top} \begin{pmatrix} \frac{\partial}{\partial t}\psi\big(t(\delta)\big)x \\ 1 \end{pmatrix} \frac{\partial}{\partial \delta} t(\delta) \end{aligned} \tag{43}$$

$$= \left[\frac{\partial}{\partial \delta}t(\delta)\right]\left[D\frac{\frac{\partial}{\partial t}\psi\big(t(\delta)\big)}{\gamma(\delta)} + \begin{pmatrix} s\big(\gamma(\delta)x, t(\delta)\big) \\ \frac{\partial}{\partial t}\log p\big(\gamma(\delta)x, t(\delta)\big)\end{pmatrix}^{\top}\begin{pmatrix}\frac{\partial}{\partial t}\psi\big(t(\delta)\big)x \\ 1\end{pmatrix}\right] \tag{44}$$

$$\begin{aligned} &= \left[\frac{\partial}{\partial \delta}t(\delta)\right]\left[\left(\frac{\partial}{\partial t}\psi\big(t(\delta)\big)\right)\left(\frac{D}{\gamma(\delta)} + \Big\langle x, s\big(\gamma(\delta)x, t(\delta)\big)\Big\rangle\right)\right. \\ &\qquad\qquad \left. + \frac{\partial}{\partial t}\log p\big(\gamma(\delta)x, t(\delta)\big)\right]. \end{aligned} \tag{45}$$

Substituting Equation 41 into Equation 45 yields:

$$\begin{aligned} \frac{\partial}{\partial \delta}\log \varrho(x,\delta) = \left[\frac{\partial}{\partial \delta}t(\delta)\right] &\left[\left(\frac{\partial}{\partial t}\psi\big(t(\delta)\big)\right)\left(\frac{D}{\gamma(\delta)} + \Big\langle x, s\big(\gamma(\delta)x, t(\delta)\big)\Big\rangle\right)\right. \\ &- \left[\nabla\cdot f\big(\gamma(\delta)x, t(\delta)\big)\right] - \Big\langle f\big(\gamma(\delta)x, t(\delta)\big), s\big(\gamma(\delta)x, t(\delta)\big)\Big\rangle \\ &\left. + \frac{1}{2}g^2\big(t(\delta)\big)\left(\mathrm{tr}\left(\nabla s\big(\gamma(\delta)x, t(\delta)\big)\right) + \left\|s\big(\gamma(\delta)x, t(\delta)\big)\right\|_2^2\right)\right]. \end{aligned} \tag{46}$$

From now on, to simplify notation, when dealing with a scalar function h, we will denote its derivative as h'. Since $t(\delta) = \lambda^{-1}(e^{\delta})$, the chain rule gives:

$$\frac{\partial}{\partial \delta}t(\delta) = \frac{e^{\delta}}{\lambda'\big(\lambda^{-1}(e^{\delta})\big)} = \frac{\lambda\big(t(\delta)\big)}{\lambda'\big(t(\delta)\big)}. \tag{47}$$

So far, we have not used that $f(x,t) = b(t)x$, which implies that $\nabla\cdot f(x,t) = Db(t)$ and that $\langle f(x,t), s(x,t)\rangle = b(t)\langle x, s(x,t)\rangle$. Using these observations and Equation 47, Equation 46 becomes:

$$\begin{aligned} \frac{\partial}{\partial \delta}\varrho(x,\delta) = \frac{\lambda\big(t(\delta)\big)}{\lambda'\big(t(\delta)\big)} &\left[\left(\frac{\psi'\big(t(\delta)\big)}{\psi\big(t(\delta)\big)} - b\big(t(\delta)\big)\right)D\right. \\ &+ \Big\langle\Big(\psi'\big(t(\delta)\big) - b\big(t(\delta)\big)\psi\big(t(\delta)\big)\Big)x, s\big(\gamma(\delta)x, t(\delta)\big)\Big\rangle \\ &\left. + \frac{1}{2}g^2\big(t(\delta)\big)\left(\mathrm{tr}\left(\nabla s\big(\gamma(\delta)x, t(\delta)\big)\right) + \left\|s\big(\gamma(\delta)x, t(\delta)\big)\right\|_2^2\right)\right]. \end{aligned} \tag{48}$$

If we showed that

$$\psi'(t) - b(t)\psi(t) = 0, \quad \text{and that} \quad \frac{\lambda(t)}{2\lambda'(t)}g^2(t) = \sigma^2(t), \tag{49}$$

then Equation 48 would simplify to Equation 12. From equation 5.50 in (Särkkä & Solin, 2019), we have that

$$\psi'(t) = b(t)\psi(t), \tag{50}$$

which shows that indeed $\psi'(t) - b(t)\psi(t) = 0$. Then, from equation 5.51 in (Särkkä & Solin, 2019), we also have that

$$\left(\sigma^2\right)'(t) = 2b(t)\sigma^2(t) + g^2(t), \tag{51}$$

and from the chain rule this gives that

$$\sigma'(t) = \frac{2b(t)\sigma^2(t) + g^2(t)}{2\sigma(t)}. \tag{52}$$

We now finish verifying Equation 49. Since $\lambda(t) = \sigma(t)/\psi(t)$, the chain rule implies that

$$\frac{\lambda(t)}{2\lambda'(t)} g^2(t) = \frac{\frac{\sigma(t)}{\psi(t)}}{\frac{\sigma'(t)\psi(t) - \sigma(t)\psi'(t)}{\psi^2(t)}} \frac{g^2(t)}{2} = \frac{\sigma(t)\psi(t)}{\sigma'(t)\psi(t) - \sigma(t)b(t)\psi(t)} \frac{g^2(t)}{2} \tag{53}$$

$$= \frac{\sigma(t)}{\sigma'(t) - b(t)\sigma(t)} \frac{g^2(t)}{2} = \frac{\sigma(t)}{\frac{2b(t)\sigma^2(t) + g^2(t)}{2\sigma(t)} - b(t)\sigma(t)} \frac{g^2(t)}{2} \tag{54}$$

$$= \frac{2\sigma^2(t)}{2b(t)\sigma^2(t) + g^2(t) - 2b(t)\sigma^2(t)} \frac{g^2(t)}{2} = \sigma^2(t), \tag{55}$$

which, as previously mentioned, shows that Equation 48 simplifies to Equation 12.

C.3. Proof of Theorem 3.1

We begin by stating and proving a lemma which we will later use.

Lemma C.1. *For any $\epsilon > 0$ and $\xi > 0$, there exists $\Delta < 0$ such that for all $\delta < \Delta$ and $y \in \mathbb{R}^d$ with $\|y\|_2 > \xi$, it holds that:*

$$\mathcal{N}(y; 0, e^{2\delta} I_d) < \epsilon e^{2\delta}. \tag{56}$$

Proof. The inequality holds if and only if

$$-\frac{d}{2}\log(2\pi) - d\delta - \frac{e^{-2\delta}\|y\|_2^2}{2} < \log \epsilon + 2\delta, \tag{57}$$

which in turn is equivalent to

$$\|y\|_2^2 > 2\left(-2\delta - \log\epsilon - \left(\delta + \frac{\log(2\pi)}{2}\right) d\right) e^{2\delta}. \tag{58}$$

The limit of the right hand side as $\delta \to -\infty$ is 0 (and it approaches from the positive side), which finishes the proof. □

We now restate Theorem 3.1 for convenience:

Theorem 3.1. *Let $\mathcal{L}$ be an embedded submanifold of $\mathbb{R}^D$ given by a d-dimensional affine subspace. If $p(\cdot, 0)$ is supported on $\mathcal{L}$, continuous, and with finite second moments, then for any $x \in \mathcal{L}$ with $p(x, 0) > 0$, we have:*

$$\lim_{\delta \to -\infty} \frac{\partial}{\partial \delta} \log \varrho(x, \delta) = d - D. \tag{15}$$

Proof. As the result is invariant to rotations and translations, we assume without loss of generality that $\mathcal{L} = \{(x', 0) \in \mathbb{R}^D \mid x' \in \mathbb{R}^d, 0 \in \mathbb{R}^{D-d}\}$. Since $x \in \mathcal{L}$, it has the form $x = (x', 0)$ for some $x' \in \mathbb{R}^d$. Note that formally $p(\cdot, 0)$ is not a density with respect to the D-dimensional Lebesgue measure, however, with a slight abuse of notation, we identify it with $p(x')$, where $p(\cdot)$ is now the d-dimensional Lebesgue density of X', where $(X', 0) = X \sim p(\cdot, 0)$. We will denote $p(\cdot) \circledast \mathcal{N}(\cdot; 0, e^{2\delta} I_d)$ as $p_\delta(\cdot)$. In this simplified notation, our assumptions are that $p(\cdot)$ is continuous at x with finite second moments, and that x is such that $p(x) > 0$.

For ease of notation we use $\mathcal{N}_d^\delta$ to represent normal distribution with variance $e^{2\delta}$ on a d-dimensional space, i.e. $\mathcal{N}_d^\delta(\cdot) = \mathcal{N}(\cdot; 0, e^{2\delta} I_d)$. For any subspace S we use S^c to denote its complement where the ambient space is clear from context. $B_\xi(0)$ denotes ball of radius ξ around the origin.

We start by noticing that the derivative of the logarithm of a Gaussian with respect to its log variance can be computed as:

$$\frac{\partial}{\partial \delta} \log \mathcal{N}_d^{\delta}(x') = \frac{\partial}{\partial \delta} \left\{ -\frac{d}{2}\log(2\pi) - d\delta - \frac{e^{-2\delta}}{2} \|x'\|_2^2 \right\} = -d + e^{-2\delta} \|x'\|_2^2 . \tag{59}$$

We then have that:

$$\varrho(x,\delta) = p_\delta(x') \times \mathcal{N}_{D-d}^{\delta}(0) \tag{60}$$
$$\implies \log \varrho(x,\delta) = \log p_\delta(x') - \delta(D-d) + c_0 \tag{61}$$
$$\implies \frac{\partial}{\partial \delta}\log \varrho(x,\delta) = \frac{\partial}{\partial \delta}\log p_\delta(x') - (D-d), \tag{62}$$

where c_0 is a constant that does not depend on δ. Thus, it suffices to show that $\lim_{\delta\to-\infty} \frac{\partial}{\partial\delta}\log p_\delta(x') = 0$:

$$\lim_{\delta\to-\infty} \frac{\partial}{\partial \delta}\log p_\delta(x') = \lim_{\delta\to-\infty} \frac{\frac{\partial}{\partial\delta} p_\delta(x')}{p_\delta(x')} \tag{63}$$
$$= \lim_{\delta\to-\infty} \frac{\frac{\partial}{\partial\delta}\int_{\mathbb{R}^d} p(x'-y)\mathcal{N}_d^{\delta}(y)\mathrm{d}y}{\int_{\mathbb{R}^d} p(x'-y)\mathcal{N}_d^{\delta}(y)\mathrm{d}y} \tag{64}$$
$$= \lim_{\delta\to-\infty} \frac{\int_{\mathbb{R}^d} p(x'-y)\frac{\partial}{\partial\delta}\mathcal{N}_d^{\delta}(y)\mathrm{d}y}{\int_{\mathbb{R}^d} p(x-y)\mathcal{N}_d^{\delta}(y)\mathrm{d}y} \tag{65}$$
$$= \lim_{\delta\to-\infty} \frac{\int_{\mathbb{R}^d} p(x'-y)(-d+e^{-2\delta}\|y\|_2^2)\mathcal{N}_d^{\delta}(y)\mathrm{d}y}{\int_{\mathbb{R}^d} p(x'-y)\mathcal{N}_d^{\delta}(y)\mathrm{d}y} \tag{66}$$
$$= -d + \lim_{\delta\to-\infty} \frac{e^{-2\delta}\int_{\mathbb{R}^d} p(x'-y)\|y\|_2^2\mathcal{N}_d^{\delta}(y)\mathrm{d}y}{\int_{\mathbb{R}^d} p(x'-y)\mathcal{N}_d^{\delta}(y)\mathrm{d}y}, \tag{67}$$

where we exchanged the order of derivation and integration in Equation 65 using Leibniz integral rule (because the normal distribution, its derivative, and p are continuous; note that p does not depend on δ so regularity on its derivative is not necessary), and where Equation 66 follows from Equation 59. Thus, proving that

$$\lim_{\delta\to-\infty} \frac{e^{-2\delta}\int_{\mathbb{R}^d} p(x'-y)\|y\|_2^2\mathcal{N}_d^{\delta}(y)\mathrm{d}y}{\int_{\mathbb{R}^d} p(x'-y)\mathcal{N}_d^{\delta}(y)\mathrm{d}y} = d \tag{68}$$

would finish our proof.

Now let $\epsilon > 0$. By continuity of p at x', there exists $\xi > 0$ such that if $\|y\|_2 < \xi$, then $|p(x'-y) - p(x')| < \epsilon$. Let Δ be the corresponding Δ from Lemma B.1. Assume $\delta < \Delta$ and define c_1 and c_2 as follows:

$$c_1 = \int_{B_\xi^c(0)} p(x'-y)\mathcal{N}_d^{\delta}(y)\mathrm{d}y, \quad \text{and} \quad c_2 = \int_{B_\xi^c(0)} p(x'-y)\|y\|_2^2(\epsilon e^{2\delta})^{-1}\mathcal{N}_d^{\delta}(y)\mathrm{d}y. \tag{69}$$

From Lemma B.1 and p having finite second moments it follows that $c_1 \in [0,1]$ and that $c_2 \in \left[0, \int_{\mathbb{R}^d}\|y\|_2^2 p(x'-y)dy\right]$. We have:

$$\frac{e^{-2\delta}\int_{\mathbb{R}^d} p(x'-y)\|y\|_2^2\mathcal{N}_d^{\delta}(y)\mathrm{d}y}{\int_{\mathbb{R}^d} p(x'-y)\mathcal{N}_d^{\delta}(y)\mathrm{d}y} = \frac{e^{-2\delta}\int_{B_\xi(0)} p(x'-y)\|y\|_2^2\mathcal{N}_d^{\delta}(y)\mathrm{d}y + c_2\epsilon}{\int_{B_\xi(0)} p(x'-y)\mathcal{N}_d^{\delta}(y)\mathrm{d}y + c_1\epsilon} \tag{70}$$
$$= \frac{e^{-2\delta}p(x')\int_{B_\xi(0)}\|y\|_2^2\mathcal{N}_d^{\delta}(y)\mathrm{d}y + e^{-2\delta}\int_{B_\xi(0)}(p(x'-y)-p(x'))\|y\|_2^2\mathcal{N}_d^{\delta}(y)\mathrm{d}y + c_2\epsilon}{p(x')\int_{B_\xi(0)}\mathcal{N}_d^{\delta}(y)\mathrm{d}y + \int_{B_\xi(0)}(p(x'-y)-p(x'))\mathcal{N}_d^{\delta}(y)\mathrm{d}y + c_1\epsilon}. \tag{71}$$

Analoguously to c_1 and c_2, there exists $c_3 \in [-1,1]$ and $c_4 \in [-d,d]$ so that the Equation 71 is equal to:

$$\frac{e^{-2\delta}\int_{B_\xi(0)}\|y\|_2^2\mathcal{N}_d^{\delta}(y)\mathrm{d}y + \frac{(c_2+c_4)\epsilon}{p(x')}}{\int_{B_\xi(0)}\mathcal{N}_d^{\delta}(y)\mathrm{d}y + \frac{(c_1+c_3)\epsilon}{p(x')}} = \frac{d - e^{-2\delta}\int_{B_\xi^c(0)}\|y\|_2^2\mathcal{N}_d^{\delta}(y)\mathrm{d}y + \frac{(c_2+c_4)\epsilon}{p(x')}}{1 - \int_{B_\xi^c(0)}\mathcal{N}_d^{\delta}(y)\mathrm{d}y + \frac{(c_1+c_3)\epsilon}{p(x')}} =: I. \tag{72}$$

We still need to prove that $\lim_{\delta\to-\infty} I = d$. Taking $\limsup$ and $\liminf$ as $\delta \to -\infty$ yields:

$$\frac{d + \frac{(c_2'+c_4')\epsilon}{p(x')}}{1 + \frac{(c_1''+c_3'')\epsilon}{p(x')}} \leq \liminf_{\delta\to-\infty} I \leq \limsup_{\delta\to-\infty} I \leq \frac{d + \frac{(c_2''+c_4'')\epsilon}{p(x')}}{1 + \frac{(c_1'+c_3')\epsilon}{p(x')}}, \tag{73}$$

where $c_i'' = \limsup_{\delta\to-\infty} c_i$ and $c_i' = \liminf_{\delta\to-\infty} c_i$. Note that although the values of c_i' and c_i'' depend on ϵ and ξ, the bounds on them do not. We can thus take the limit of this inequality as ξ and ϵ approach zero:

$$d \leq \lim_{\epsilon,\xi\to 0} \liminf_{\delta\to-\infty} I \leq \lim_{\epsilon,\xi\to 0} \limsup_{\delta\to-\infty} I \leq d. \tag{74}$$

However, note that every step up to here has been an equality, therefore

$$I = \frac{e^{-2\delta} \int_{\mathbb{R}^d} p(x'-y) \left\|y\right\|_2^2 \mathcal{N}_d^\delta(y)\mathrm{d}y}{\int_{\mathbb{R}^d} p(x'-y)\mathcal{N}_d^\delta(y)\mathrm{d}y}, \tag{75}$$

so that I does not depend on ϵ nor on ξ. In turn, this implies that

$$d \leq \liminf_{\delta\to-\infty} I \leq \limsup_{\delta\to-\infty} I \leq d \implies \lim_{\delta\to-\infty} I = d, \tag{76}$$

which finishes the proof. □

Table 4: Essential hyperparameter settings for the Diffusion models with MLP backbone.

Property	Model Configuration
Learning rate	10^{-4}
Optimizer	`AdamW`
Scheduler	Cosine scheduling with 500 warmup steps (von Platen et al., 2022)
Epochs	200, 400, 800, or 1000 based on the ambient dimension
Score-matching loss	Likelihood weighting (Song et al., 2021a)
SDE drift	$f(x,t) := -\frac{1}{2}\beta(t)x$
SDE diffusion	$g(t) := \sqrt{\beta(t)}$
$\beta(t)$	Linear interpolation: $\beta(t) := 0.1 + 20t$
Score network	MLP
MLP hidden sizes	$\langle 4096, 2048, 2\times 1024, 3\times 512, 2\times 1024, 2048, 4096\rangle$
Time embedding size	128

D. Experimental Details

Throughout all our experiments, we used an NVIDIA A100 GPU with 40GB of memory.

D.1. DM Hyperparameter Setup

Throughout our experiments, we use an MLP architecture with a bottleneck as our score network: $2\times L+1$ fully connected layers with dimensions $\langle h_1, h_2, \ldots, h_L, \ldots h_{2L+1}\rangle$ forming a bottleneck, i.e., h_L has the smallest size. Notably, for $1 \le i \le L$, the ith transform connects layer $i-1$ (or the input) to layer i with a linear transform of dimensions "$h_{i-1} \times h_i$", and the $(L+i)$th layer (or the output) not only contains input from the $(L+i-1)$th layer but also, contains skip connections from layer $(L-i)$ (or the input), thus forming a linear transform of dimension "$(h_{L+i-1} + h_{L-i}) \times h_{L+i}$". For image experiments, we scale and shift the pixel intensities to be zero-centered with a standard deviation of 1. In addition, we embed times $t \in (0,1)$ using the scheme in (von Platen et al., 2022) and concatenate with the input before passing to the score network. All hyperparameters are summarized in Table 4.

D.2. FLIPD Estimates and Curves for Synthetic Distributions

Figure 5 shows pointwise LID estimates for a lollipop distribution taken from (Tempczyk et al., 2022). It is a uniform distribution over three submanifolds: (i) a 2-d candy, (ii) a 1-d stick, and (iii) an isolated point of zero-dimensions. Note that the FLIPD estimates at $t_0 = 0.05$ for all three submanifolds are coherent.

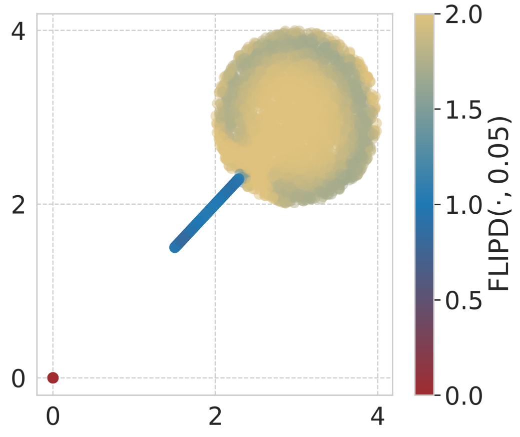

Figure 5: The FLIPD estimates on a Lollipop taken from (Tempczyk et al., 2022).

Figure 6 shows the FLIPD curve as training progresses on the lollipop example and the Gaussian mixture that was already discussed in Section 4. We see that gradually, knee patterns emerge at the correct LID, indicating that the DM is learning the data manifold. Notably, data with higher LID values get assigned higher estimates *even after a few epochs*, demonstrating that FLIPD effectively ranks data based on LID, even when the DM is underfitted.

Finally, Figure 7 presents a summary of complex manifolds obtained from neural spline flows and high-dimensional mixtures, showing knees around the true LID.

D.3. A Simple Multiscale Experiment

Tempczyk et al. (2022) argue that when setting δ, all the directions of data variation that have a log standard deviation below

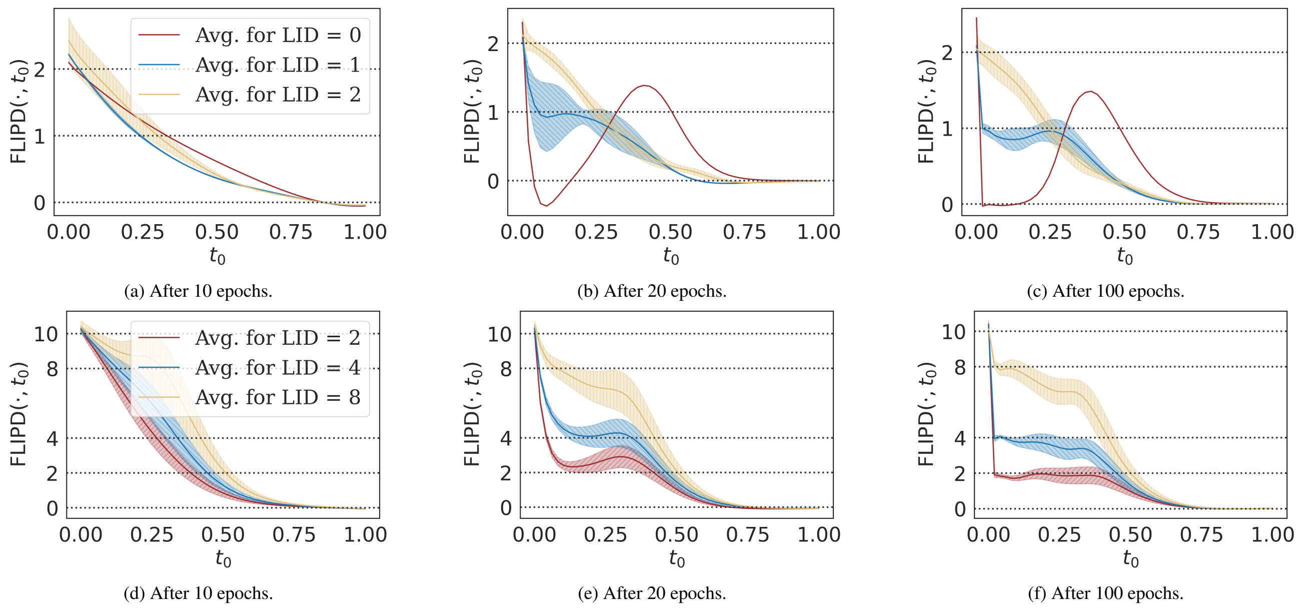

(a) After 10 epochs. (b) After 20 epochs. (c) After 100 epochs.

(d) After 10 epochs. (e) After 20 epochs. (f) After 100 epochs.

Figure 6: The evolution of the FLIPD curve while training the DM to fit a Lollipop (top) and a manifold mixture $\mathcal{N}_2 + \mathcal{N}_4 + \mathcal{N}_8 \subseteq \mathbb{R}^{10}$ (bottom).

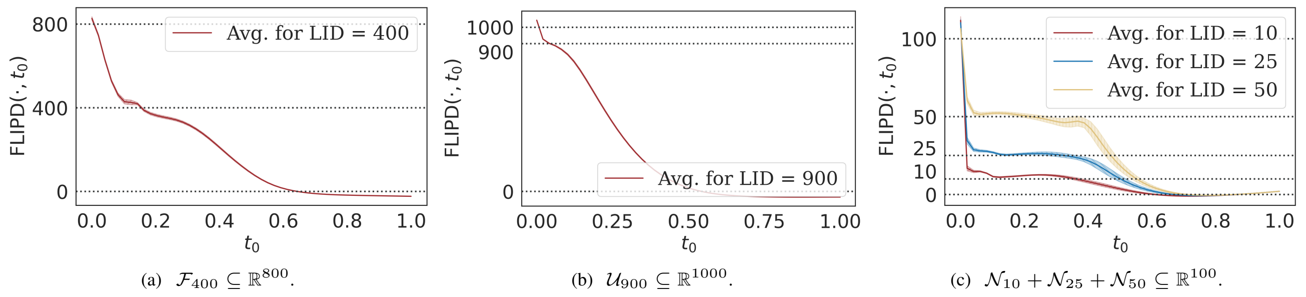

(a) $\mathcal{F}_{400} \subseteq \mathbb{R}^{800}$. (b) $\mathcal{U}_{900} \subseteq \mathbb{R}^{1000}$. (c) $\mathcal{N}_{10} + \mathcal{N}_{25} + \mathcal{N}_{50} \subseteq \mathbb{R}^{100}$.

Figure 7: The FLIPD curve for complex and high-dimensional manifolds.

δ are ignored. Here, we make this connection more explicit.

We define a multivariate Gaussian distribution with a prespecified eigenspectrum for its covariance matrix: having three eigenvalues of 10^{-4}, three eigenvalues of 1, and four eigenvalues of 10^3. This ensures that the distribution is numerically 7-d and that the directions and amount of data variation are controlled using the eigenvectors and eigenvalues of the covariance matrix.

For this multivariate Gaussian, the score function in Equation 12 can be written in closed form; thus, we evaluate FLIPD both with and without training a DM. We see in Figure 8 the estimates obtained in both scenarios match closely, with some deviations due to imperfect model fit, which we found matches perfectly when training for longer.

Apart from the initial knee at 7, which is expected, we find another at $t_0 = 0.6$ (corresponding to $e^\delta \approx 6.178$ with our hyperparameter setup in Table 4) where the value of FLIPD is 4. This indeed confirms that the estimator focuses solely on the 4-d space characterized by the eigenvectors having eigenvalues of 10^3, and by ignoring the eigenvalues 10^{-4} and 1 which are both smaller than 6.178.

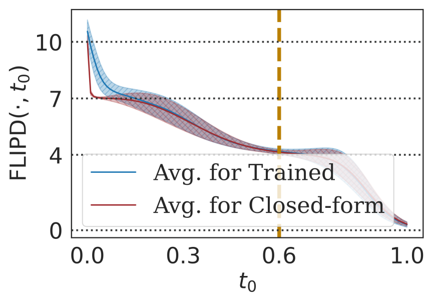

Figure 8: FLIPD curve for a multivariate Gaussian with controlled covariance eigenspectrum.

D.4. In-depth Analysis of the Synthetic Benchmark

Generating Manifold Mixtures To create synthetic data, we generate each component of our manifold mixture separately and then join them to form a distribution. All mixture components are sampled with equal probability in the final distribution. For a component with the intrinsic dimension of d, we first sample from a base distribution in d dimensions. This base distribution is isotropic Gaussian and Laplace for $\mathcal{N}_d$ and $\mathcal{L}_d$ and uniform for the case of $\mathcal{U}_d$ and $\mathcal{F}_d$. We then zero-pad these samples to match the ambient dimension D and perform a random $D \times D$ rotation on $\mathbb{R}^D$ (each component has one such transformation). For $\mathcal{F}_d$, we have an additional step to make the submanifold complex. We first initialize a neural spline flow (using the `nflows` library (Durkan et al., 2020)) with 5 coupling transforms, 32 hidden layers, 32 hidden blocks, and tail bounds of 10. The data is then passed through the flow, resulting in a complex manifold embedded in $\mathbb{R}^D$ with an LID of d. Finally, we standardize each mixture component individually and set their modes such that the pairwise Euclidean distance between them is at least 20. We then translate each component so its barycenter matches the corresponding mode, ensuring that data from different components rarely mixes, thus maintaining distinct LIDs.

LIDL Baseline Following the hyperparameter setup in (Tempczyk et al., 2022), we train 8 models with different noised-out versions of the dataset with standard deviations $e^{\delta_i} \in \{0.01, 0.014, 0.019, 0.027, 0.037, 0.052, 0.072, 0.1\}$. The normalizing flow backbone is taken from (Durkan et al., 2020), using 10 piecewise rational quadratic transforms with 32 hidden dimensions, 32 blocks, and a tail bound of 10. While (Tempczyk et al., 2022) uses an autoregressive architecture, we use coupling transforms for increased training efficiency and to match the training time of a single DM.

Setup We use model-free estimators from the `skdim` library (Bac et al., 2021) and across our experiments, we sample 10^6 points from the synthetic distributions for either fitting generative models or fitting the model-free estimators. We then evaluate LID estimates on a uniformly subsampled set of 2^{12} points from the original set of 10^6 points. Some methods are relatively slow, and this allows us to have a fair, yet feasible comparison. We do not see a significant difference even when we double the size of the subsampled set. We focus on four different model-free baselines for our evaluation: ESS (Johnsson et al., 2014), LPCA (Fukunaga & Olsen, 1971; Cangelosi & Goriely, 2007), MLE (Levina & Bickel, 2004; MacKay & Ghahramani, 2005), and FIS (Albergante et al., 2019), all with default settings. Note that FIS does not scale beyond 100 dimensions. Computing pairwise distances on high dimensions ($D \geq 800$) on all 10^6 samples takes over 24 hours even with 40 CPU cores. Therefore, for $D \geq 800$, we use the same 2^{12} subsamples we use for evaluation.

Evaluation We have three tables to summarize our analysis: (i) Table 6 shows the MAE of the LID estimates, comparing each datapoint's estimate to the ground truth at a fine-grained level; (ii) Table 7 shows the average LID estimate for synthetic manifolds with only one component, this average is typically used to estimate *global* intrinsic dimensionality in baselines; finally, (iii) looks at the concordance index (Harrell Jr et al., 1996) of estimates for cases with multiple submanifolds of different dimensionalities. Concordance indices for a sequence of LID estimates $\{\widehat{\text{LID}}\}_{n=1}^N$ are formally defined as follows:

$$\mathcal{C}\left(\{\text{LID}_n\}_{n=1}^N, \{\widehat{\text{LID}}_n\}_{n=1}^N\right) = \sum_{\substack{1\leq n_1 \neq n_2 \leq N \\ \text{LID}_{n_1} \leq \text{LID}_{n_2}}} \mathbb{I}(\widehat{\text{LID}}_{n_1} \leq \widehat{\text{LID}}_{n_2}) / \binom{N}{2} \tag{77}$$

where $\mathbb{I}$ is the indicator function; a perfect estimator will have a $\mathcal{C}$ of 1. Instead of emphasizing the actual values of the LID estimates, this metric assesses how well the ranks of an estimator align with those of ground truth (Steck et al., 2007; Mayr & Petras, 2008; Teles, 2012; Kamkari et al., 2024a), thus evaluating LID as a "relative" measure of complexity.

Model-free Analysis Among model-free methods, LPCA and ESS show good performance in low dimensions (with LPCA being exceptionally good) but falter as dimensions increase. As we see in Table 6, while model-free methods outperform other estimators when $D < 100$, as D increases the paradigm shifts with model-based estimators outperforming the model-free ones. In addition, as shown in Table 7, all model-free baselines underestimate intrinsic dimensionality to some degree, with LPCA and MLE being particularly drastic for $D \geq 800$. We note that ESS performs relatively well, even beating model-based methods in some 800-dimensional scenarios. However, we note that the $\mathcal{C}$ values in Table 8 suggest it cannot rank data by LID as effectively as even the least performant MLE estimator.

Model-based Analysis Moving to model-based methods, we see in Table 8 that all perform poorly in ranking data based on LID except our FLIPD estimator. Remarkably, FLIPD achieves perfect $\mathcal{C}$ values among *all* datasets; further justifying it as a relative measure of complexity. We also note that while LIDL and NB provide better global estimates in Table 7 for

Table 5: MAE (lower is better). Rows show synthetic manifolds and columns represent different variations of our Fokker-Planck-based estimators.

Synthetic Manifold	FLIPD	FLIPD	FPRegress	FPRegress
	$t_0 = .05$	`kneedle`	`kneedle`	$\delta_1 = -1$
Lollipop in $\mathbb{R}^2$	**0.142**	0.419	0.572	0.162
String within doughnut $\mathbb{R}^3$	**0.052**	0.055	0.398	0.377
Swiss Roll in $\mathbb{R}^3$	**0.053**	0.055	0.087	0.161
$\mathcal{L}_5 \subseteq \mathbb{R}^{10}$	**0.100**	0.169	1.168	0.455
$\mathcal{N}_{90} \subseteq \mathbb{R}^{100}$	0.501	**0.492**	3.142	0.998
$\mathcal{U}_{10} + \mathcal{U}_{30} + \mathcal{U}_{90} \subseteq \mathbb{R}^{100}$	3.140	**1.298**	5.608	10.617
$\mathcal{F}_{10} + \mathcal{F}_{25} + \mathcal{F}_{50} \subseteq \mathbb{R}^{100}$	14.37	**3.925**	16.32	21.01
$\mathcal{U}_{10} + \mathcal{U}_{80} + \mathcal{U}_{200} \subseteq \mathbb{R}^{800}$	39.54	**14.30**	30.06	29.99

high dimensions, they have worse MAE performance in Table 6. This once again suggests that at a local level, our estimator is superior compared to others, beating all baselines in 2 out of 3 groups of synthetic manifolds with $D \geq 100$ in Table 6. Finally, we see a curious flipped behaviour with NB estimators where they perform better when increasing dimensionality.

D.5. Ablations

We begin by evaluating the impact of using `kneedle`. Our findings, summarized in Table 5, indicate that while setting a small fixed t_0 is effective in low dimensions, the advantage of `kneedle` becomes particularly evident as the number of dimensions increases.

Additionally, experiments in Table 5 suggest that Theorem 3.1 holds in the non-linear case as well. We introduce "FPRegress", an estimator derived from the method discussed in Section 3.2. The key idea is that if the $\mathcal{O}(1)$ term depends on δ such that the derivative of $\log \varrho(x, \delta)$ with respect to δ skews the estimator significantly, then FLIPD may not be reliable. Since Theorem 3.1 confirms this is not the case only for affine manifolds, it is reasonable to ablate this aspect.

Recall that to obtain LIDL estimates, one must solve Equation 13 m times for a set of log standard deviations $\delta_1 < \ldots < \delta_m$. For a given origin δ_1, we set $\delta_i = i \times \delta_1$ and use Euler's method with $m - 1$ steps to get $\log \hat{\varrho}(x, \delta_i)$ for $1 \leq i \leq 8$. Finally, a regression similar to LIDL is used to extract the LID estimate. This estimator is not only slower than FLIPD, but as we see in Table 5, it has worse MAEs.

We also tried combining it with `kneedle` by sweeping over the origin δ_1 and arguing that the estimates obtained from this method also exhibit knees. Despite some improvement in high-dimensional settings, Table 5 shows that even coupling it with `kneedle` does not help.

D.6. Improving the NB Estimators with `kneedle`

We recall that the NB estimator requires computing $\operatorname{rank} S(x)$, where $S(x)$ is a $K \times D$ matrix formed by stacking the scores $\hat{s}(\cdot, t_0)$. We set $t_0 = 0.01$ as it provides the most reasonable estimates. To compute $\operatorname{rank} S(x)$ numerically, (Stanczuk et al., 2022) perform a singular value decomposition on $S(x)$ and use a cutoff threshold τ below which singular values are considered zero. Finding the best τ is challenging, so Stanczuk et al. (2022) propose finding the two consecutive singular values with the maximum gap. Furthermore, we see that sometimes the top few singular values are disproportionately higher than the rest, resulting in severe overestimations of the LID. Thus, we introduce an alternative algorithm to determine the optimal τ. For each τ, we estimate LID by thresholding the singular values. Sweeping 100 different τ values from 0 to 1000 at a geometric scale (to further emphasize smaller thresholds) produces estimates ranging from D (keeping all singular values) to 0 (ignoring all). As τ varies, we see that the estimates plateau over a certain range of τ. We use `kneedle` to detect this plateau because the starting point of a plateau is indeed a knee in the curve. This significantly improves the baseline, especially in high dimensions: see the third column of Tables 6, 7, and 8 compared to the second column.

Table 6: MAE (lower is better). Each row represents a synthetic dataset and each column represents an LID estimation method. Rows are split into groups based on the ambient dimension: the first group of rows shows toy examples; the second shows low-dimensional data with $D = 10$; the third shows moderate-dimensional data with $D = 100$; and the last two show high-dimensional data with $D = 800$ and $D = 1000$, respectively.

Synthetic Manifold	FLIPD `kneedle`	NB Vanilla	NB `kneedle`	LIDL	ESS	LPCA	MLE	FIS
Lollipop in $\mathbb{R}^2$	0.419	0.577	0.855	0.052	0.009	**0.000**	0.142	0.094
Swiss Roll in $\mathbb{R}^3$	0.055	0.998	0.016	0.532	0.017	**0.000**	0.165	0.018
Doughnut Mixture in $\mathbb{R}^3$	0.055	1.475	0.414	1.104	0.017	**0.000**	0.128	0.041
Summary (Toy Manifolds)	0.176	1.017	0.428	0.563	0.014	**0.000**	0.145	0.051
$\mathcal{N}_5 \subseteq \mathbb{R}^{10}$	0.084	5.000	0.005	0.071	0.061	**0.000**	0.441	0.206
$\mathcal{L}_5 \subseteq \mathbb{R}^{10}$	0.169	1.000	0.146	0.101	0.068	**0.000**	0.462	0.203
$\mathcal{U}_5 \subseteq \mathbb{R}^{10}$	0.324	4.994	0.933	0.123	0.153	**0.000**	0.451	0.186
$\mathcal{F}_5 \subseteq \mathbb{R}^{10}$	0.666	1.216	0.765	0.487	0.168	**0.000**	0.497	0.176
$\mathcal{N}_2 + \mathcal{N}_4 + \mathcal{N}_8 \subseteq \mathbb{R}^{10}$	0.287	5.706	1.078	0.308	0.156	**0.000**	0.406	0.206
$\mathcal{L}_2 + \mathcal{L}_4 + \mathcal{L}_8 \subseteq \mathbb{R}^{10}$	0.253	5.708	0.772	0.515	0.193	**0.001**	0.437	0.018
$\mathcal{U}_2 + \mathcal{U}_4 + \mathcal{U}_8 \subseteq \mathbb{R}^{10}$	0.586	5.677	3.685	0.363	0.331	**0.115**	0.540	0.222
$\mathcal{F}_2 + \mathcal{F}_4 + \mathcal{F}_8 \subseteq \mathbb{R}^{10}$	0.622	5.709	2.187	1.013	0.428	**0.115**	0.642	0.269
Summary (10-dimensional)	0.066	0.381	0.161	0.211	0.005	**0.000**	0.054	0.019
$\mathcal{U}_{10} \subseteq \mathbb{R}^{100}$	0.910	30.115	0.000	1.370	0.644	**0.000**	1.263	–
$\mathcal{U}_{30} \subseteq \mathbb{R}^{100}$	0.505	50.521	0.000	0.542	1.465	**0.002**	7.622	–
$\mathcal{U}_{90} \subseteq \mathbb{R}^{100}$	0.640	1.157	1.327	**0.332**	2.034	21.90	39.65	–
$\mathcal{N}_{30} \subseteq \mathbb{R}^{100}$	0.887	52.43	**0.000**	0.892	0.534	**0.000**	5.703	–
$\mathcal{N}_{90} \subseteq \mathbb{R}^{100}$	0.492	**0.184**	2.693	0.329	1.673	21.88	39.45	–
$\mathcal{F}_{80} \subseteq \mathbb{R}^{100}$	**1.869**	20.00	3.441	1.871	3.660	16.78	34.41	–
$\mathcal{U}_{10} + \mathcal{U}_{25} + \mathcal{U}_{50} \subseteq \mathbb{R}^{100}$	**0.868**	57.96	0.890	5.869	4.988	6.749	16.12	–
$\mathcal{U}_{10} + \mathcal{U}_{30} + \mathcal{U}_{90} \subseteq \mathbb{R}^{100}$	**1.298**	61.58	1.482	8.460	21.89	20.06	41.05	–
$\mathcal{N}_{10} + \mathcal{N}_{25} + \mathcal{N}_{50} \subseteq \mathbb{R}^{100}$	1.813	74.20	**0.555**	8.873	7.712	5.716	14.37	–
$\mathcal{F}_{10} + \mathcal{F}_{25} + \mathcal{F}_{50} \subseteq \mathbb{R}^{100}$	**3.925**	74.20	6.205	18.61	9.200	6.769	16.78	–
Summary (100-dimensional)	**1.321**	42.24	1.659	4.715	5.380	9.986	21.64	–
$\mathcal{U}_{200} \subseteq \mathbb{R}^{800}$	11.54	600.0	7.205	55.98	**5.116**	104.7	139.5	–
$\mathcal{F}_{400} \subseteq \mathbb{R}^{800}$	20.46	400.0	**10.15**	207.2	26.18	301.0	312.5	–
$\mathcal{U}_{10} + \mathcal{U}_{80} + \mathcal{U}_{200} \subseteq \mathbb{R}^{800}$	14.30	715.3	18.82	120.7	**2.349**	33.69	57.19	–
Summary (800-dimensional)	15.43	571.8	12.06	128.0	**11.22**	146.5	169.7	-
$\mathcal{N}_{900} \subseteq \mathbb{R}^{1000}$	**3.913**	100.0	24.38	10.45	76.40	801.0	774.4	–
$\mathcal{U}_{100} \subseteq \mathbb{R}^{1000}$	12.81	900.0	62.68	12.65	**2.055**	28.09	59.62	–
$\mathcal{U}_{900} \subseteq \mathbb{R}^{1000}$	12.81	100.0	**0.104**	24.90	75.17	801.0	762.2	–
$\mathcal{F}_{500} \subseteq \mathbb{R}^{1000}$	**21.77**	500.0	52.19	341.3	38.63	401.0	401.6	–
Summary (1000-dimensional)	**12.83**	400.0	34.84	97.33	48.06	507.8	499.5	–

Table 7: Average LID for manifolds with a single global intrinsic dimension. Rows represent uni-dimensional datasets and each column represents an LID estimation method.

Synthetic Manifold	FLIPD `kneedle`	NB Vanilla	NB `kneedle`	LIDL	ESS	LPCA	MLE	FIS
Swiss Roll in $\mathbb{R}^3$	2.012	2.998	1.984	2.527	2.008	**2.000**	2.013	2.003
$\mathcal{N}_5 \subseteq \mathbb{R}^{10}$	5.017	10.00	4.995	5.067	5.004	**5.000**	5.108	5.187
$\mathcal{L}_5 \subseteq \mathbb{R}^{10}$	4.968	6.000	4.854	5.089	4.985	**5.000**	5.123	5.182
$\mathcal{U}_5 \subseteq \mathbb{R}^{10}$	4.796	9.994	4.067	5.107	4.880	**5.000**	4.833	5.152
$\mathcal{F}_5 \subseteq \mathbb{R}^{10}$	4.722	6.216	4.461	5.482	4.890	**5.000**	4.829	5.131
$\mathcal{U}_{10} \subseteq \mathbb{R}^{100}$	11.68	40.12	10.00	11.29	9.361	**10.00**	8.905	–
$\mathcal{U}_{30} \subseteq \mathbb{R}^{100}$	31.01	80.52	30.00	30.08	28.54	**29.99**	22.38	–
$\mathcal{U}_{90} \subseteq \mathbb{R}^{100}$	89.54	91.16	91.32	**90.24**	88.27	68.10	50.35	–
$\mathcal{N}_{30} \subseteq \mathbb{R}^{100}$	30.79	82.43	30.00	30.85	29.67	**30.00**	24.38	–
$\mathcal{N}_{90} \subseteq \mathbb{R}^{100}$	89.88	90.18	92.62	**90.21**	88.89	68.12	50.55	–
$\mathcal{F}_{80} \subseteq \mathbb{R}^{100}$	77.97	100.0	83.23	**81.46**	76.35	63.22	45.59	–
$\mathcal{U}_{200} \subseteq \mathbb{R}^{800}$	211.5	800.0	**207.2**	256.0	195.3	95.30	60.51	–
$\mathcal{F}_{400} \subseteq \mathbb{R}^{800}$	454.7	800.0	**410.1**	607.2	373.8	99.00	87.53	–
$\mathcal{N}_{900} \subseteq \mathbb{R}^{1000}$	**890.3**	1000.	924.4	924.4	823.6	99.00	125.6	–
$\mathcal{U}_{100} \subseteq \mathbb{R}^{1000}$	135.76	1000.	162.7	112.6	**98.41**	71.91	40.38	–
$\mathcal{U}_{900} \subseteq \mathbb{R}^{1000}$	864.9	1000.	**900.1**	911.85	824.8	99.00	137.8	–
$\mathcal{F}_{500} \subseteq \mathbb{R}^{1000}$	582.7	1000.	**552.2**	841.3	461.4	99.00	98.38	–

Table 8: Concordance index (higher is better with 1.000 being the gold standard). Each row represents a mixture of multi-dimensional manifolds, and each column represents an LID estimation method. This table evaluates how accurately different estimators rank datapoints based on their LID.

Synthetic Manifold	FLIPD `kneedle`	NB Vanilla	NB `kneedle`	LIDL	ESS	LPCA	MLE	FIS
Lollipop in $\mathbb{R}^2$	**1.000**	0.426	0.394	0.999	**1.000**	**1.000**	**1.000**	**1.000**
Doughnut Mixture in $\mathbb{R}^3$	**1.000**	0.483	0.486	0.565	**1.000**	**1.000**	**1.000**	**1.000**
$\mathcal{N}_2 + \mathcal{N}_4 + \mathcal{N}_8 \subseteq \mathbb{R}^{10}$	**1.000**	0.341	0.725	0.943	**1.000**	**1.000**	**1.000**	**1.000**
$\mathcal{L}_2 + \mathcal{L}_4 + \mathcal{L}_8 \subseteq \mathbb{R}^{10}$	**1.000**	0.342	0.752	0.884	**1.000**	**1.000**	**1.000**	**1.000**
$\mathcal{U}_2 + \mathcal{U}_4 + \mathcal{U}_8 \subseteq \mathbb{R}^{10}$	**1.000**	0.334	0.462	0.903	**1.000**	**1.000**	**1.000**	**1.000**
$\mathcal{F}_2 + \mathcal{F}_4 + \mathcal{F}_8 \subseteq \mathbb{R}^{10}$	**1.000**	0.342	0.578	0.867	**1.000**	**1.000**	0.999	**1.000**
$\mathcal{U}_{10} + \mathcal{U}_{25} + \mathcal{U}_{50} \subseteq \mathbb{R}^{100}$	**1.000**	0.467	0.879	0.759	0.855	0.897	**1.000**	–
$\mathcal{U}_{10} + \mathcal{U}_{30} + \mathcal{U}_{90} \subseteq \mathbb{R}^{100}$	**1.000**	0.342	0.826	0.742	0.742	0.855	**1.000**	–
$\mathcal{N}_{10} + \mathcal{N}_{25} + \mathcal{N}_{50} \subseteq \mathbb{R}^{100}$	**1.000**	0.342	0.866	0.736	0.878	0.917	**1.000**	–
$\mathcal{F}_{10} + \mathcal{F}_{25} + \mathcal{F}_{50} \subseteq \mathbb{R}^{100}$	**1.000**	0.342	0.731	0.695	0.847	0.897	**1.000**	–
$\mathcal{U}_{10} + \mathcal{U}_{80} + \mathcal{U}_{200} \subseteq \mathbb{R}^{800}$	**1.000**	0.342	0.841	0.697	**1.000**	**1.000**	**1.000**	–

E. Image Experiments

E.1. FLIPD Curves and DM Samples

Figures 9 and 10 show DM-generated samples and the associated LID curves for 4096 subsamples of the datasets. In Figure 10, the FLIPD curves with MLPs, which have clearly-discernible knees as predicted by the theory, are more reasonable than those generated with UNets. The fact that FLIPD estimates are worse for UNets is surprising given that MLPs produce worse-looking samples, as shown in Figure 9. However, comparing the first and second rows of Figure 9, it also becomes clear that MLP-generated images still match some characteristics of the true dataset, suggesting that they may still be capturing the image manifold in useful ways. To explain the surprisingly poor FLIPD estimates of UNets, we hypothesize that the convolutional layers in the UNet provide some inductive biases which, while helpful to produce visually pleasing images, might also encourage the network to over-fixate on high-frequency features which are not visually perceptible. For example, Kirichenko et al. (2020) showed how normalizing flows over-fixate on these features, and how this can cause them to assign large likelihoods to out-of-distribution data, even when the model produces visually convincing samples. We hypothesize that a similar underlying phenomenon might be at play here, and that DMs with UNets might be over-emphasizing "high-frequency" directions of variation in their LID estimates, even if they learn the semantic ones and thus produce pleasing images. However, an exploration of this hypothesis is outside the scope of our work, and we highlight once again that FLIPD remains a useful measure of complexity when using UNets.

E.2. UNet Architecture

We utilize UNet architectures from the `diffusers` library (von Platen et al., 2022). The DM setup mirrors that in Table 4 except for the score backbone. For greyscale images, we employ a convolutional block followed by two attention-based downsampling blocks. The channel sizes are 128, 256, and 256, respectively. For colour images, we use two convolutional downsampling blocks (each with 128 channels), followed by two attention downsampling blocks (each with 256 channels). In both cases, these blocks are inverted using their mirrored upsampling counterparts.

E.3. Images Sorted by FLIPD

Figures 11, 12, 13, and 14 show 4096 samples of CIFAR10, SVHN, MNIST, and FMNIST sorted according to their FLIPD estimate, showing a gradient transition from the least complex datapoints (e.g., the digit 1 in MNIST) to the most complex ones (e.g., the digit 8 in MNIST). We use MLPs for greyscales and UNets for colour images but see similar trends when switching between backbones.

E.4. How Many Hutchinson Samples are Needed?

Figure 15 compares the Spearman's rank correlation coefficient between FLIPD estimates while we use $k \in \{1, 50\}$ Hutchinson samples vs. computing the trace deterministically with D Jacobian-vector-products. We see that: (i) Hutchinson sampling is particularly well-suited for UNet backbones, having generally higher correlations compared to their MLP counterparts; (ii) as t_0 increases, the correlation becomes smaller, suggesting that the Hutchinson sample complexity increases at larger timescales; (iii) for small t_0, even one Hutchinson sample is enough to estimate LID; (iv) for the UNet backbone, 50 Hutchinson samples are enough and have a high correlation (larger than 0.8) even for t_0 as large as 0.5.

E.5. Multiscale Analysis on Images

Figure 16 shows the correlation of FLIPD estimates with PNG compression for $t_0 \in (0, 1)$, indicating a consistently high correlation at small t_0, and a general decrease while increasing t_0. In addition, we see that UNet backbones correlate better with PNG.

Figures 17, 19, 21, and 23 show images with smallest and largest FLIPD estimates at different values of t_0 for the UNet backbone and Figures 18, 20, 22, and 24 show the same for the MLP backbone: (i) we see a clear difference in the complexity of top and bottom FLIPD estimates, especially for smaller t_0; this difference becomes less distinct as t_0 increases; (ii) interestingly, even for larger t_0 values with smaller PNG correlations, we qualitatively observe a clustering of the most complex datapoints at the end; however, the characteristic of this clustering changes. For example, see Figure 17 at $t_0 = 0.3$ or Figure 22 and Figure 24 at $t_0 = 0.8$, suggesting that FLIPD focuses on more coarse-grained measures of complexity at these scales; and finally (iii) while MLP backbones underperform in sample generation, their orderings are more meaningful, even showing coherent visual clustering up to $t = 0.8$ in all Figures 18, 20, 22, and 24.

E.6. Stable Diffusion

To test FLIPD with Stable Diffusion v1.5 (Rombach et al., 2022), which is known to have been finetuned on a subset of LAION-Aesthetics, we sampled 1600 images from LAION-Aesthetics-650k and computed FLIPD scores for each.

We ran FLIPD with $t_0 \in \{0.01, 0.1, 0.3, 0.8\}$ and a single Hutchinson trace sample. In all cases, FLIPD ranking clearly corresponded to complexity, though we decided upon $t_0 = 0.3$ as best capturing the "semantic complexity" of image contents. All 1600 images for $t = 0.3$ are depicted in Figure 25. For all timesteps, we show previews of the 8 lowest- and highest-LID images in Figure 26. Note that LAION is essentially a collection of URLs, and some are outdated. For the comparisons in Figure 26 and Figure 4c, we remove placeholder icons or blank images, which likely correspond to images that, at the time of writing this paper, have been removed from their respective URLs and which are generally given among the lowest LIDs.

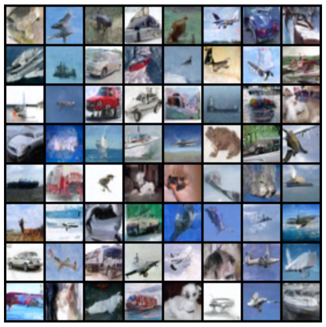
(a) CIFAR10 with UNet backbone.

(b) SVHN with UNet backbone.

(c) MNIST with UNet backbone.

(d) FMNIST with UNet backbone.

(e) CIFAR10 with MLP backbone.

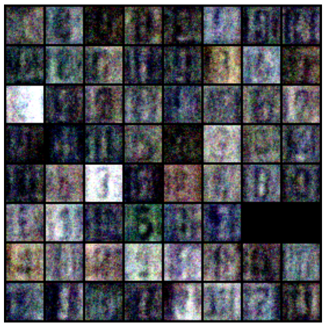
(f) SVHN with MLP backbone.

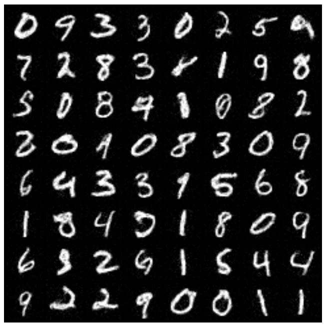
(g) MNIST with MLP backbone.

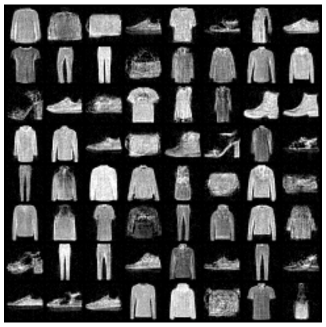
(h) FMNIST with MLP backbone.

Figure 9: Samples from DMs with different score network backbones, using the same seed for control. Despite the variation in backbones, images of the same cell in the grid (comparing top and bottom rows) show rough similarities, especially on CIFAR10 and SVHN.

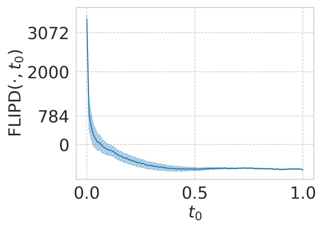

(a) CIFAR10 with UNet backbone.

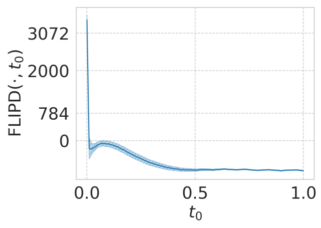

(b) SVHN with UNet backbone.

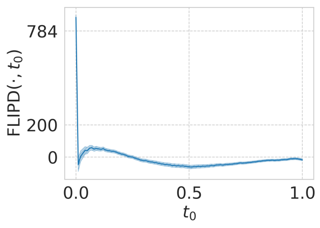

(c) MNIST with UNet backbone.

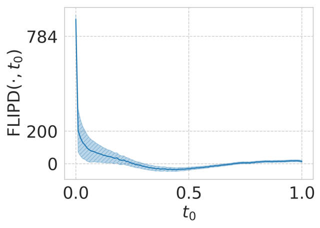

(d) FMNIST with UNet backbone.

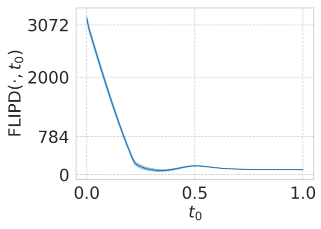

(e) CIFAR10 with MLP backbone.

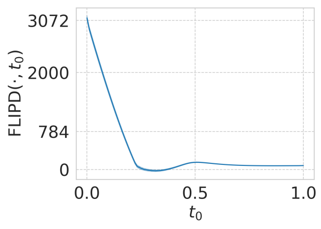

(f) SVHN with MLP backbone.

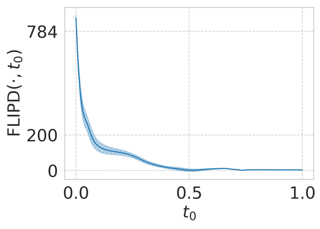

(g) MNIST with MLP backbone.

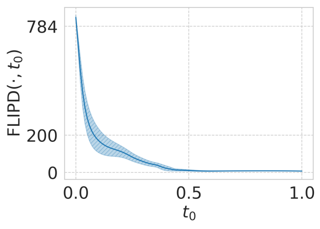

(h) FMNIST with MLP backbone.

Figure 10: FLIPD curves from all the different DMs with different score network backbones.

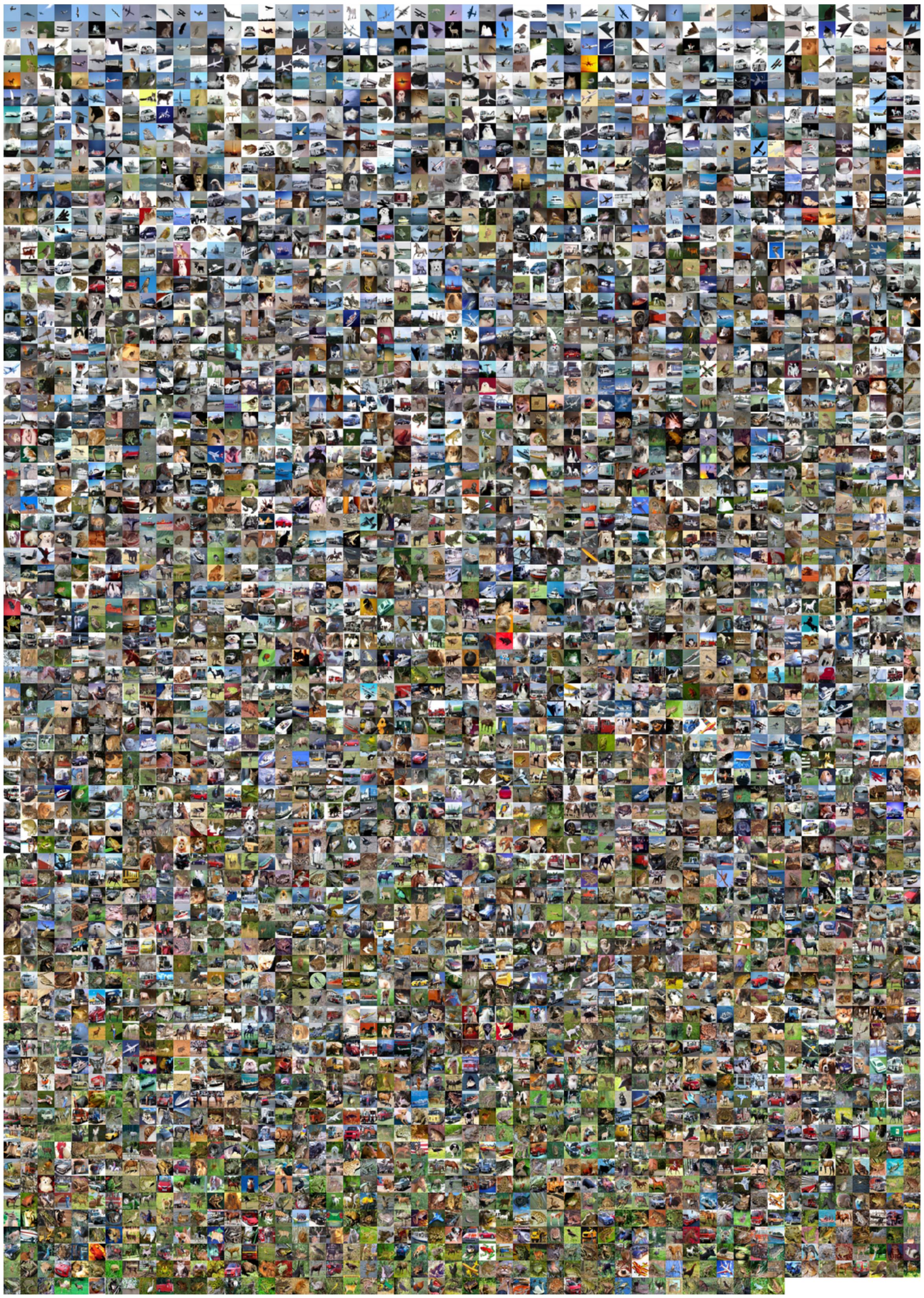

Figure 11: CIFAR10 sorted (left to right and top to bottom) by FLIPD estimate (UNet) at $t_0 = 0.01$.

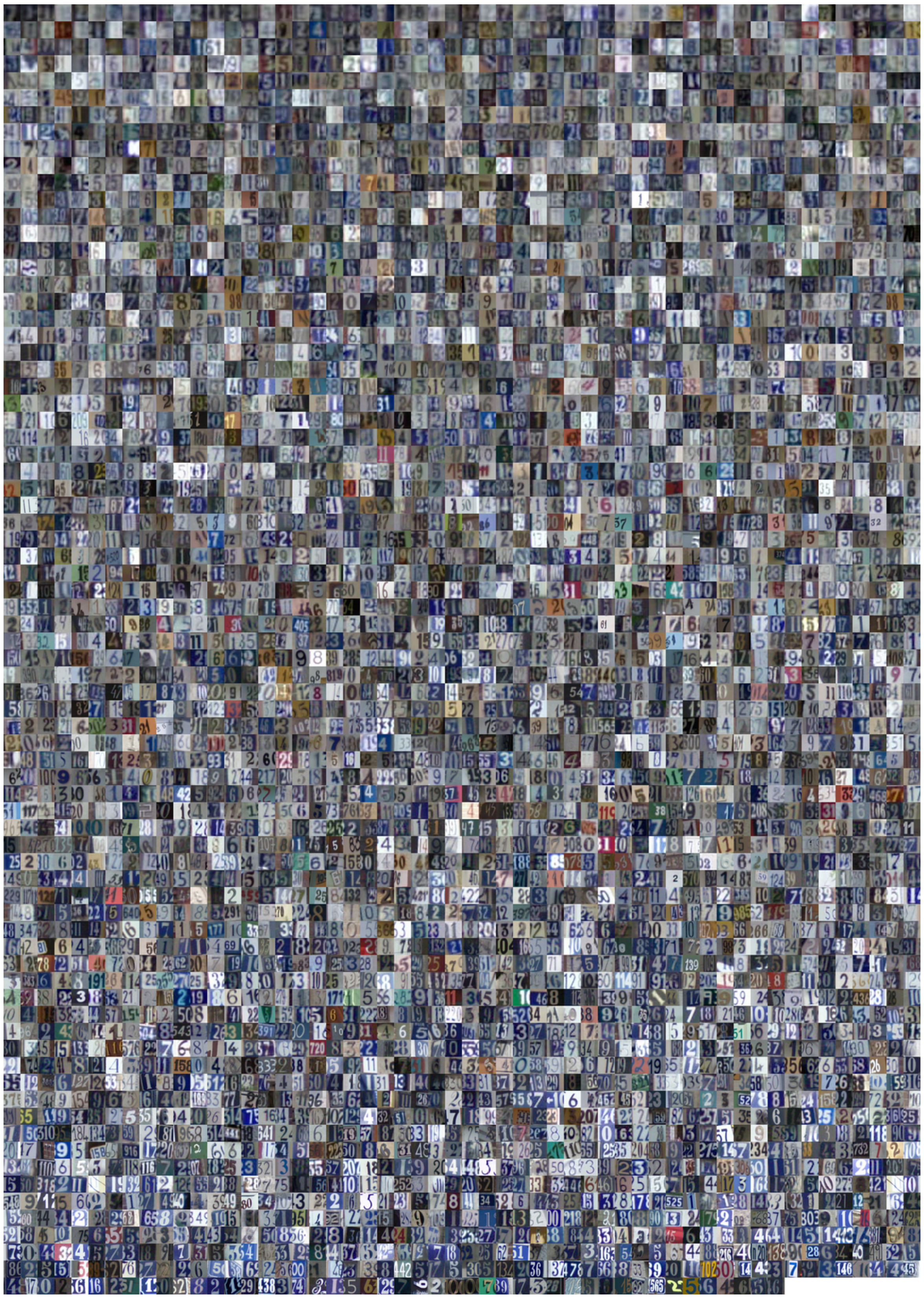

Figure 12: SVHN sorted (left to right and top to bottom) by FLIPD estimate (UNet) at $t_0 = 0.01$.

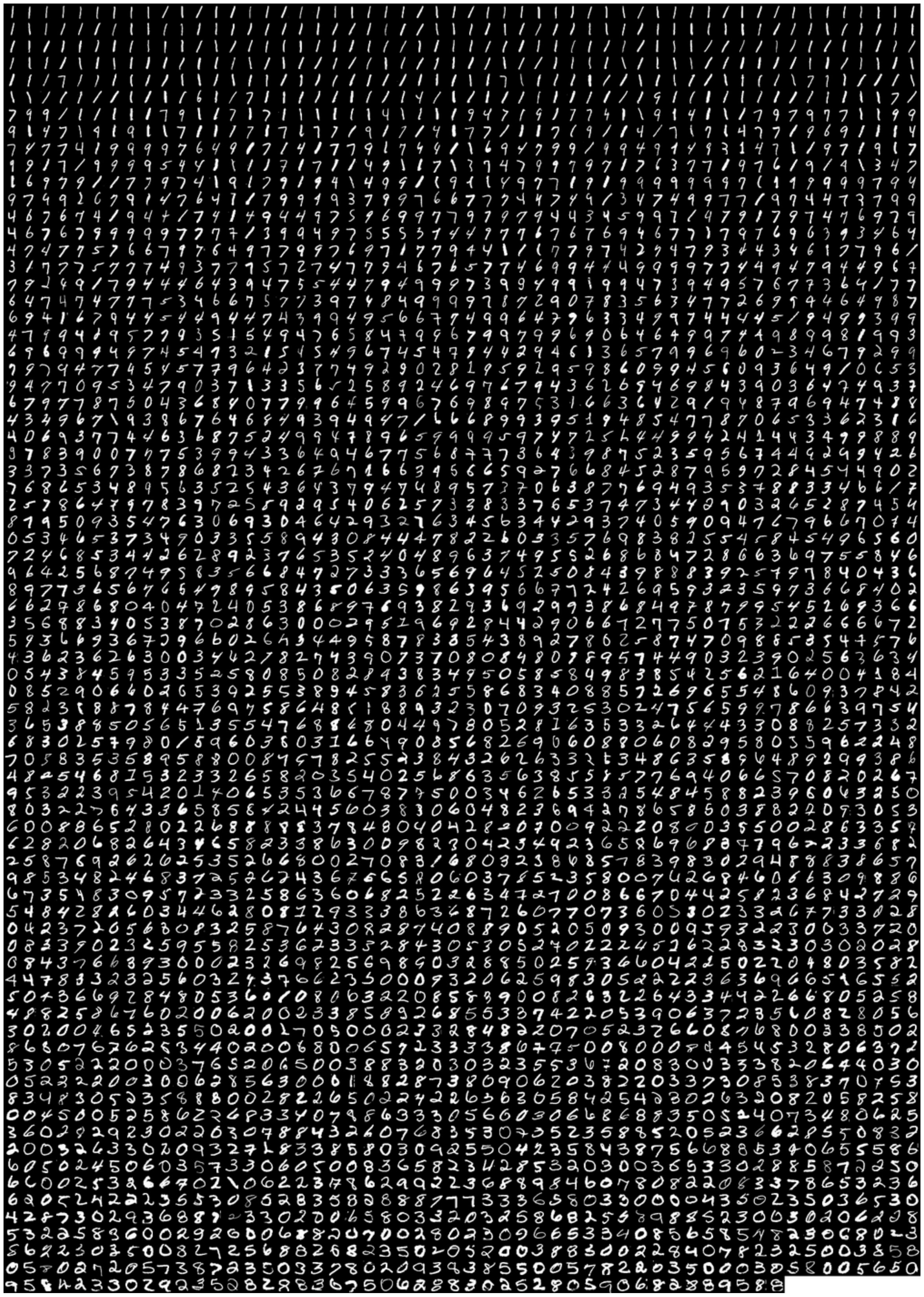

Figure 13: MNIST sorted (left to right and top to bottom) by FLIPD estimate (MLP) at $t_0 = 0.1$.

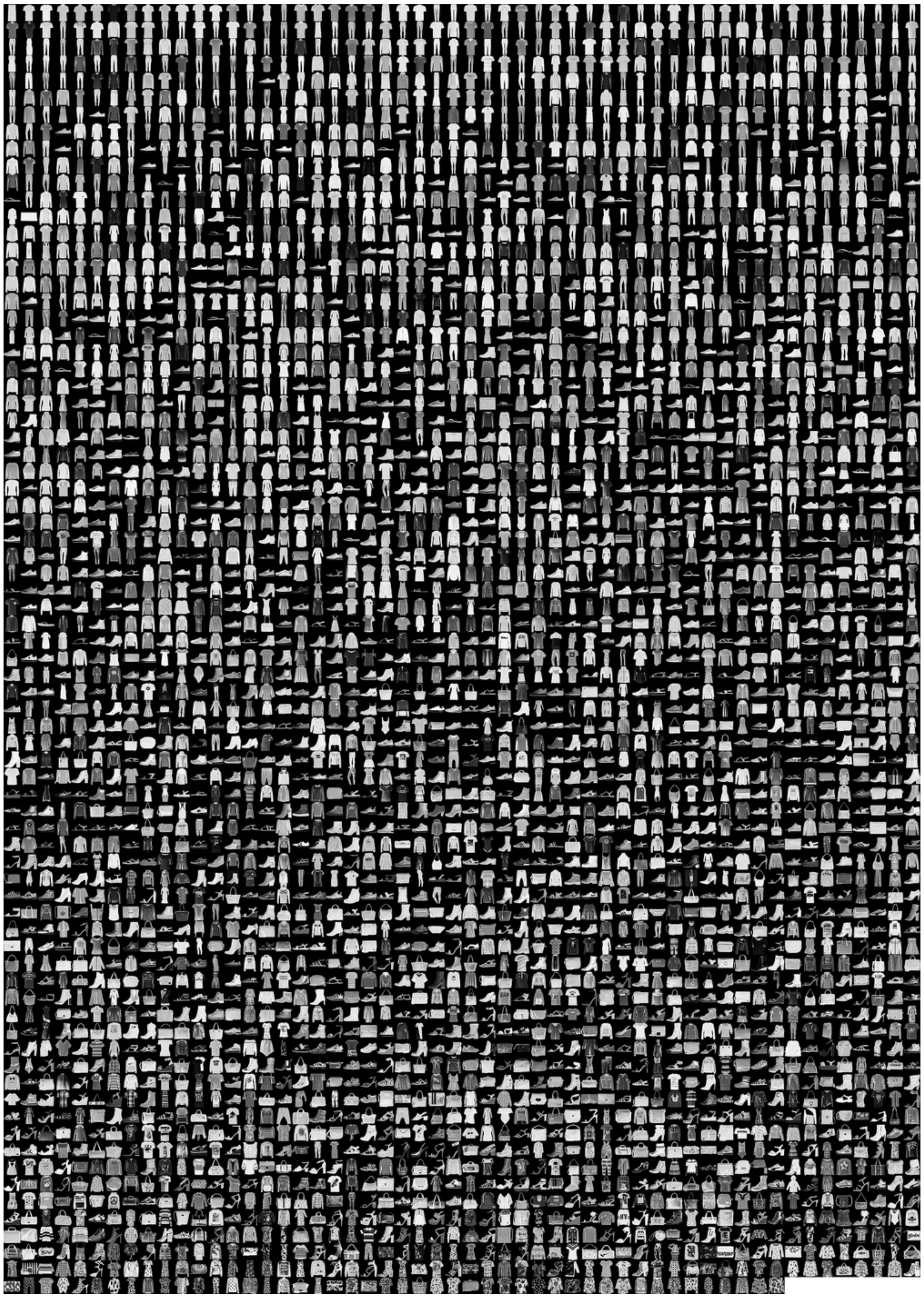

Figure 14: FMNIST sorted (left to right and top to bottom) by FLIPD estimate (MLP) at $t_0 = 0.1$.

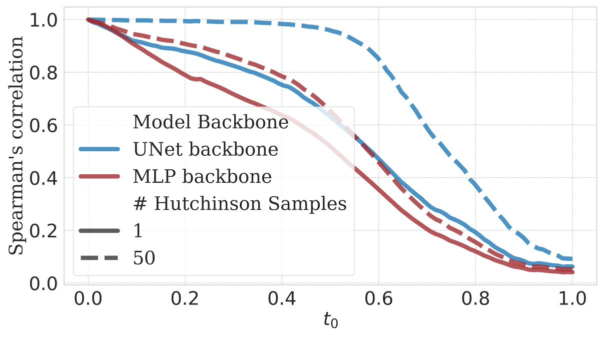

(a) Multiscale Spearman's correlation on CIFAR10.

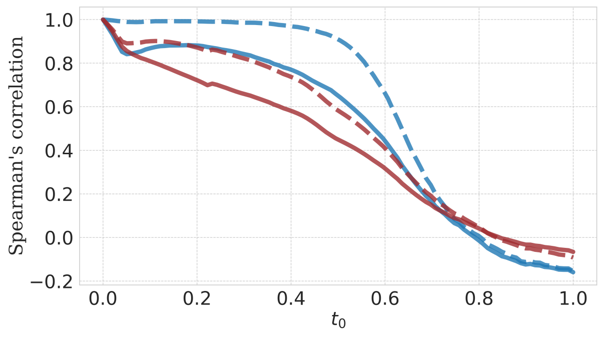

(b) Multiscale Spearman's correlation on SVHN.

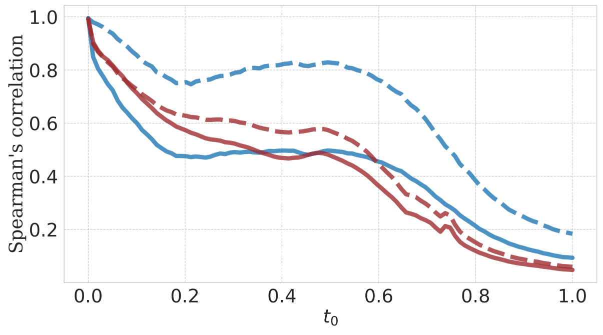

(c) Multiscale Spearman's correlation on MNIST.

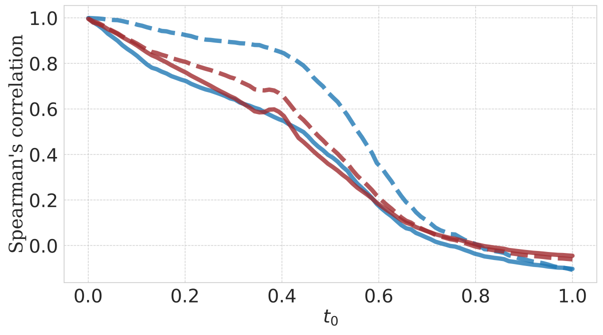

(d) Multiscale Spearman's correlation on FMNIST.

Figure 15: Spearman's correlation of FLIPD estimates while using different numbers of Hutchinson samples compared to computing the trace term of FLIPD deterministically with D Jacobian vector product calls. These estimates are evaluated at different values of $t_0 \in (0, 1)$ on four datasets using the UNet and MLP backbones.

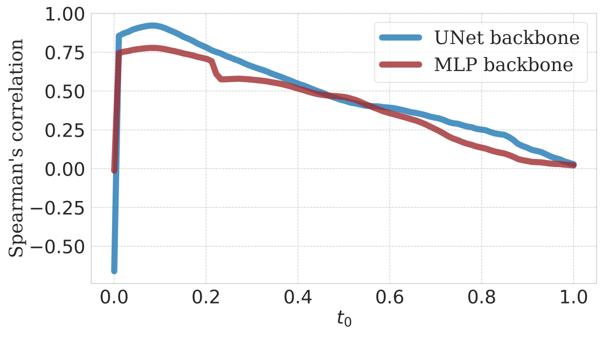

(a) Multiscale correlation with PNG on CIFAR10.

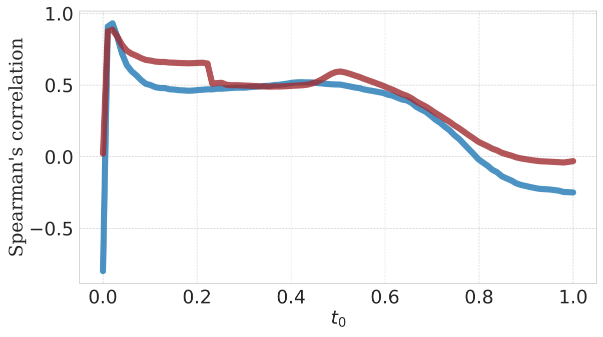

(b) Multiscale correlation with PNG on SVHN.

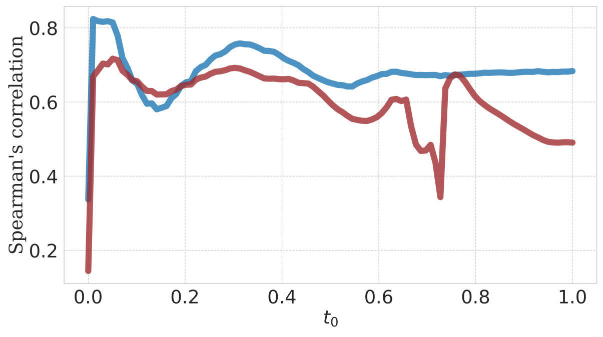

(c) Multiscale correlation with PNG on MNIST.

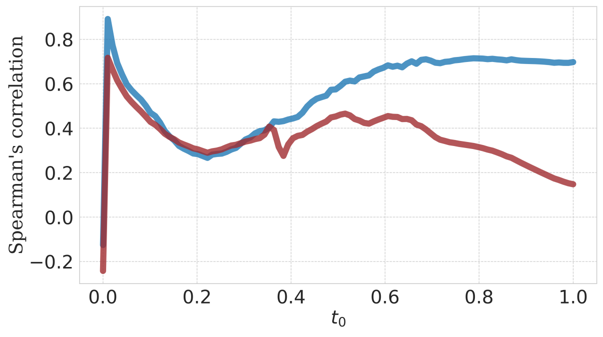

(d) Multiscale correlation with PNG on FMNIST.

Figure 16: Spearman's correlation of FLIPD estimates with PNG as we sweep $t_0 \in (0, 1)$ on different backbones and different image datasets.

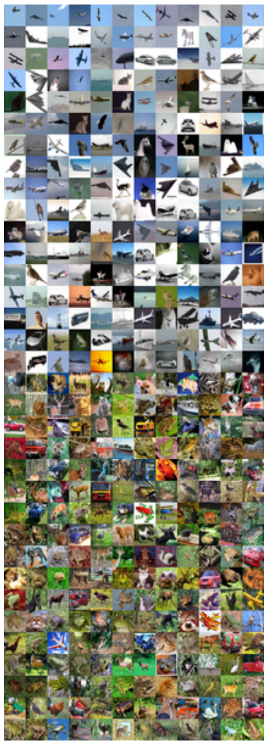
(a) $t_0 = 0.01$.

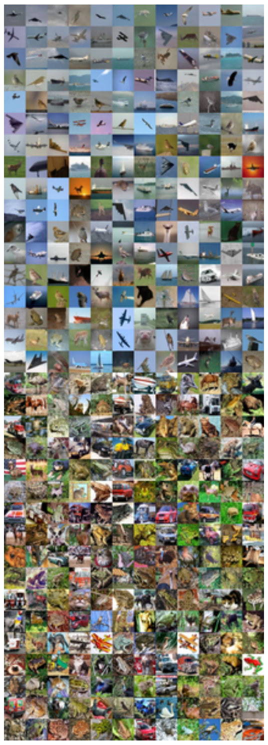
(b) $t_0 = 0.1$.

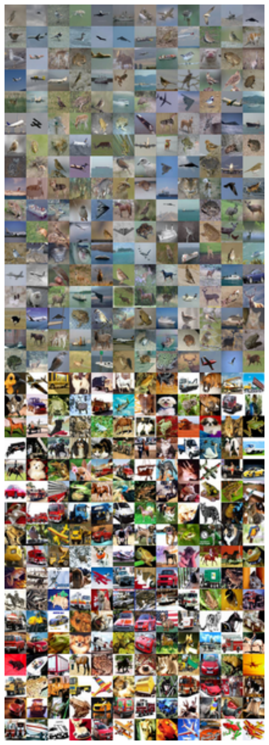
(c) $t_0 = 0.3$.

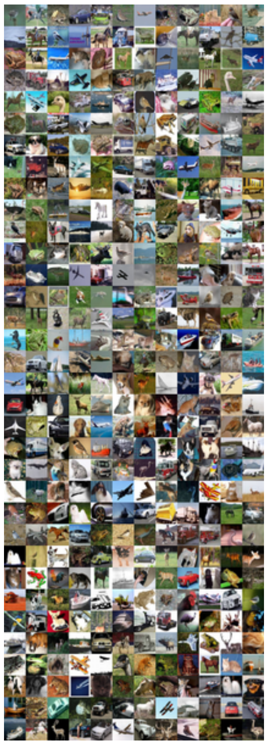
(d) $t_0 = 0.8$.

Figure 17: The 204 smallest (top) and 204 largest (bottom) CIFAR10 FLIPD estimates with UNet evaluated at different t_0.

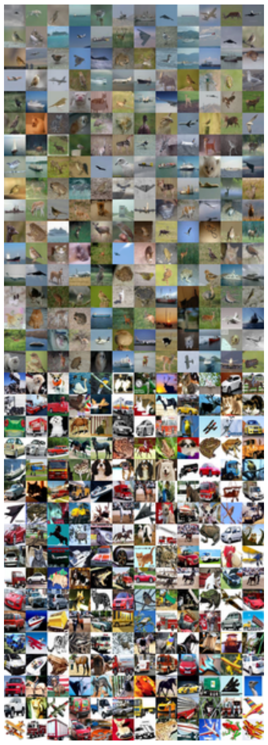
(a) $t_0 = 0.01$.

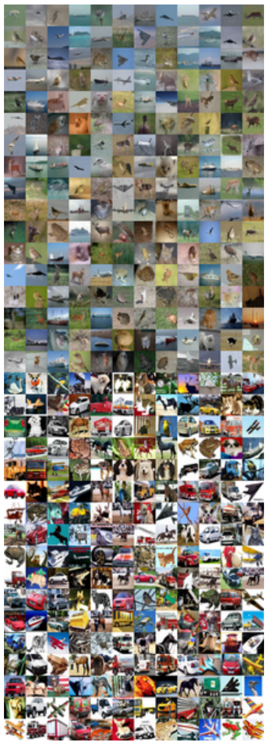
(b) $t_0 = 0.1$.

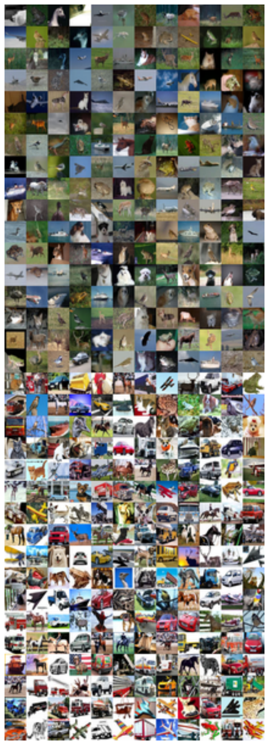
(c) $t_0 = 0.3$.

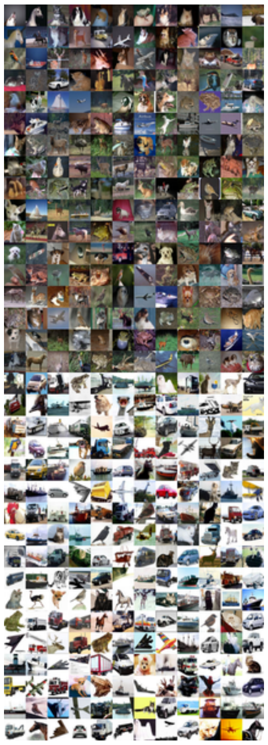
(d) $t_0 = 0.8$.

Figure 18: The 204 smallest (top) and 204 largest (bottom) CIFAR10 FLIPD estimates with MLP evaluated at different t_0.

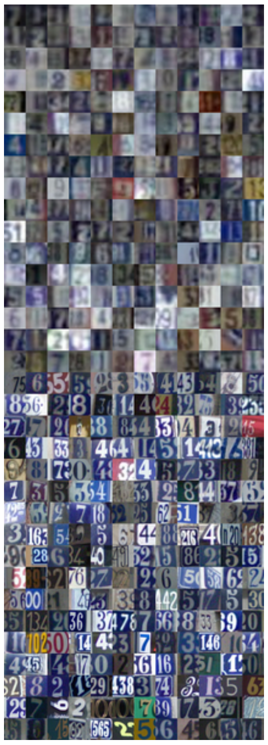
(a) $t_0 = 0.01$.

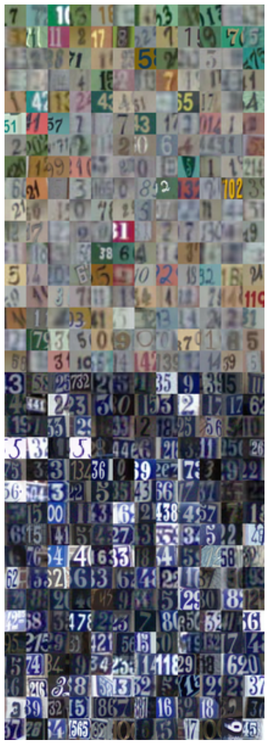
(b) $t_0 = 0.1$.

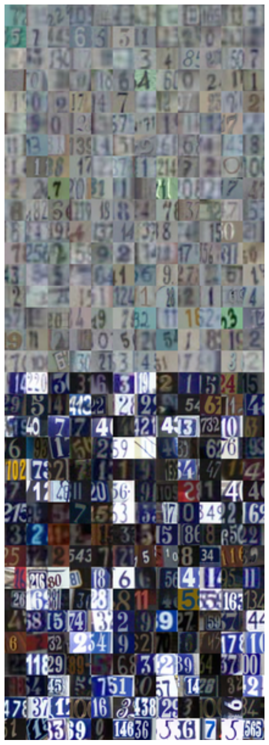
(c) $t_0 = 0.3$.

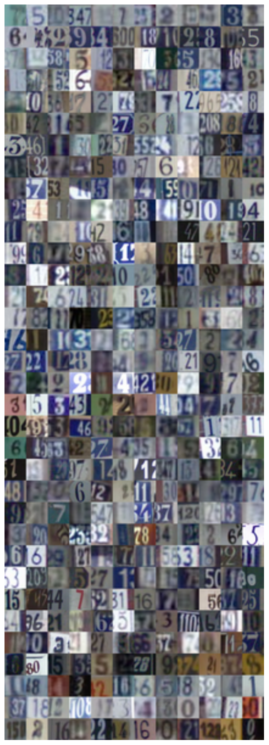
(d) $t_0 = 0.8$.

Figure 19: The 204 smallest (top) and 204 largest (bottom) SVHN FLIPD with UNet estimates evaluated at different t_0.

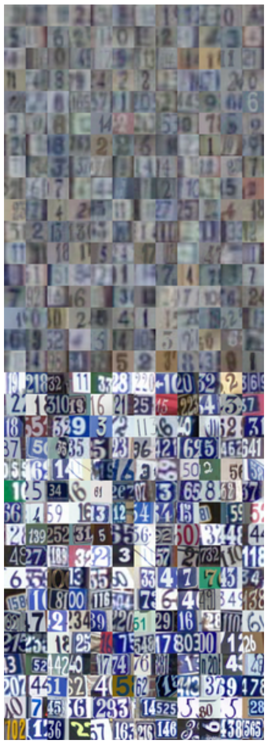
(a) $t_0 = 0.01$.

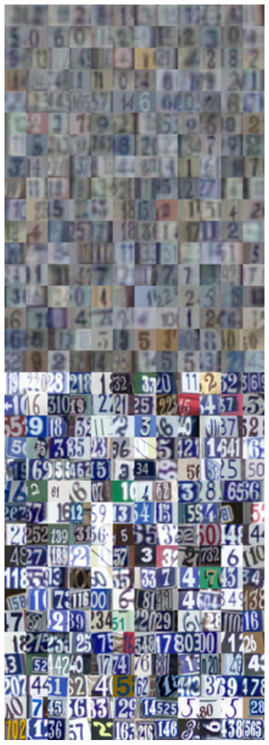
(b) $t_0 = 0.1$.

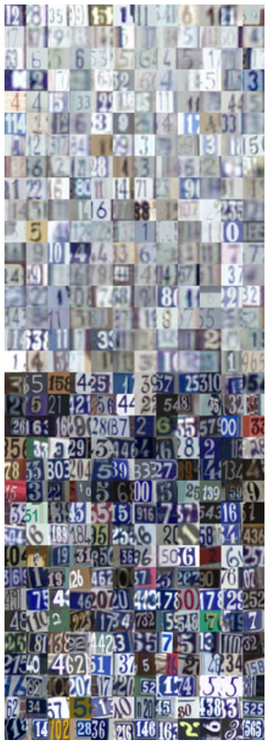
(c) $t_0 = 0.3$.

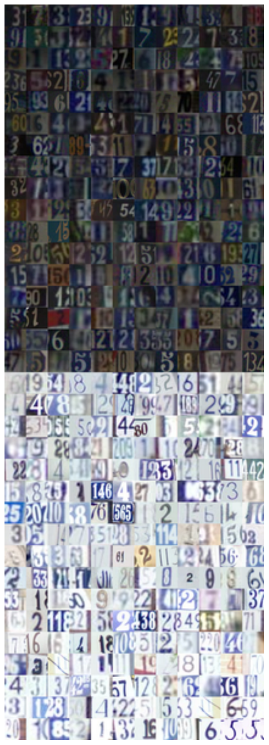
(d) $t_0 = 0.8$.

Figure 20: The 204 smallest (top) and 204 largest (bottom) SVHN FLIPD with MLP estimates evaluated at different t_0.

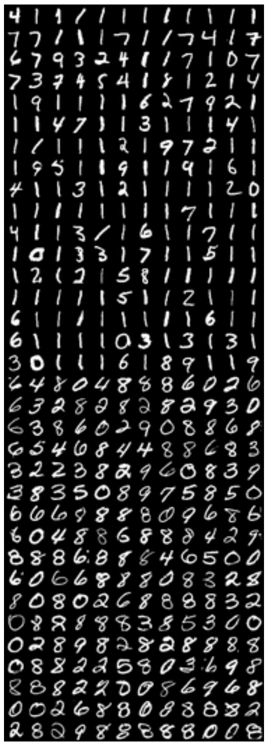
(a) $t_0 = 0.01$.

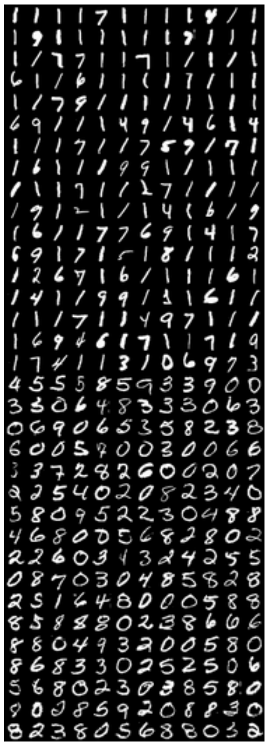
(b) $t_0 = 0.1$.

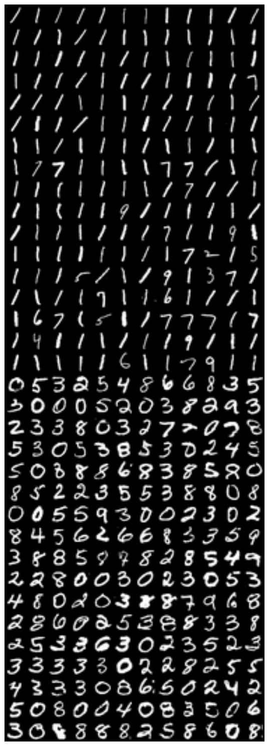
(c) $t_0 = 0.3$.

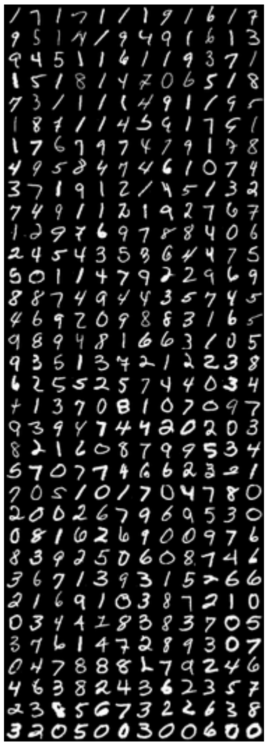
(d) $t_0 = 0.8$.

Figure 21: The 204 smallest (top) and 204 largest (bottom) MNIST FLIPD with UNet estimates evaluated at different t_0.

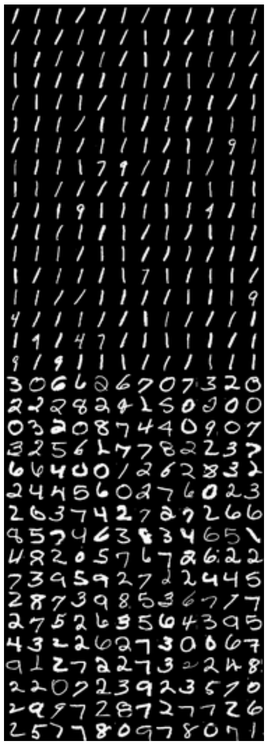
(a) $t_0 = 0.01$.

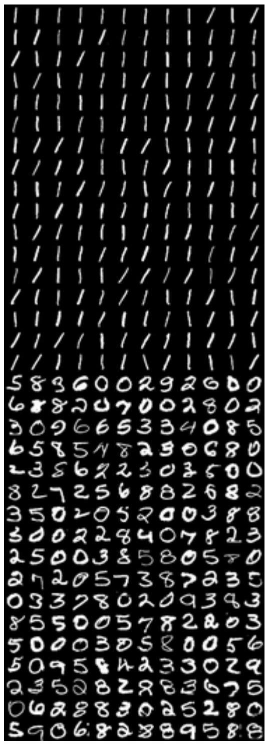
(b) $t_0 = 0.1$.

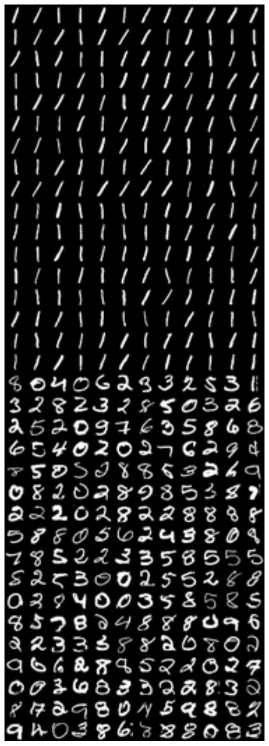
(c) $t_0 = 0.3$.

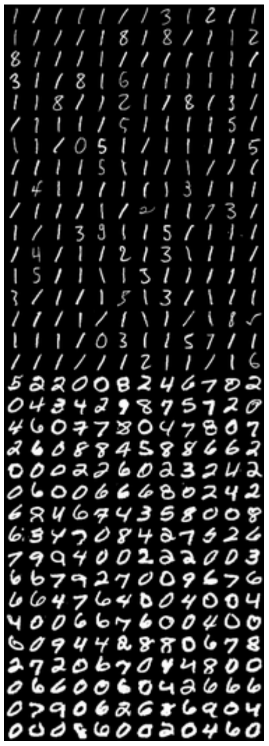
(d) $t_0 = 0.8$.

Figure 22: The 204 smallest (top) and 204 largest (bottom) MNIST FLIPD with MLP estimates evaluated at different t_0.

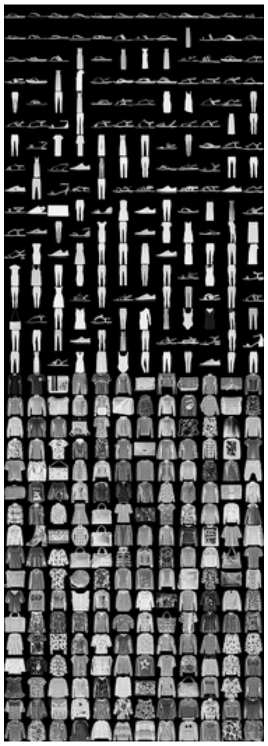
(a) $t_0 = 0.01$.

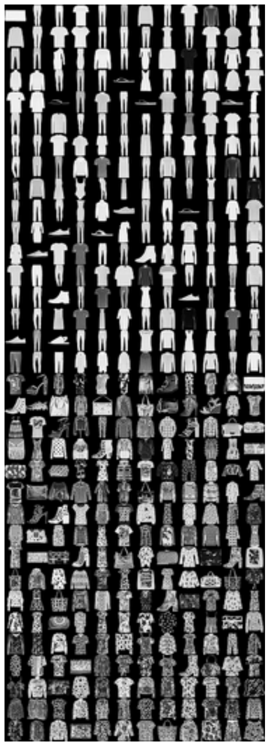
(b) $t_0 = 0.1$.

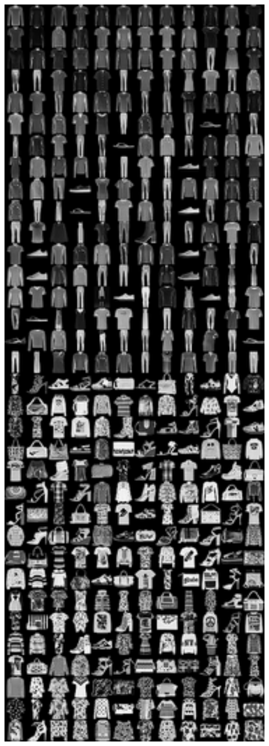
(c) $t_0 = 0.3$.

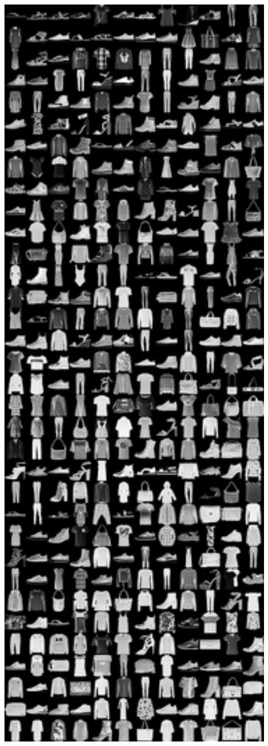
(d) $t_0 = 0.8$.

Figure 23: The 204 smallest (top) and 204 largest (bottom) FMNIST FLIPD estimates with UNet evaluated at different t_0.

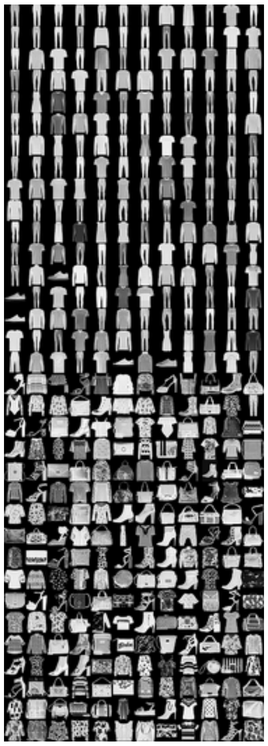
(a) $t_0 = 0.01$.

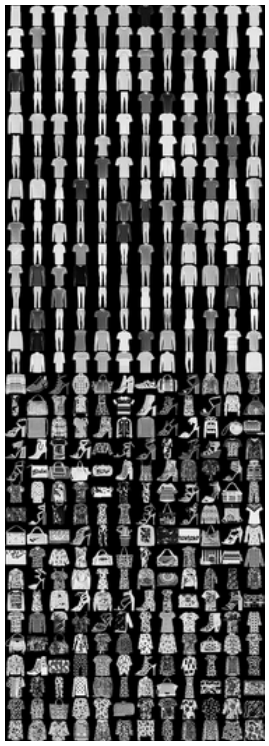
(b) $t_0 = 0.1$.

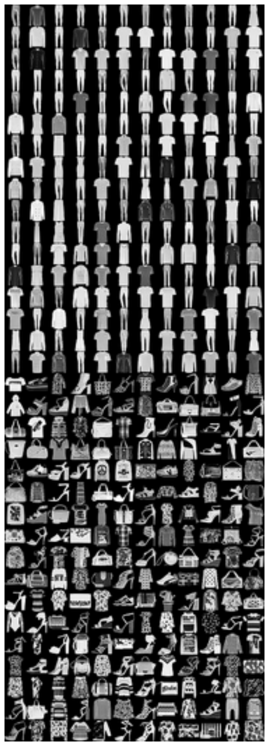
(c) $t_0 = 0.3$.

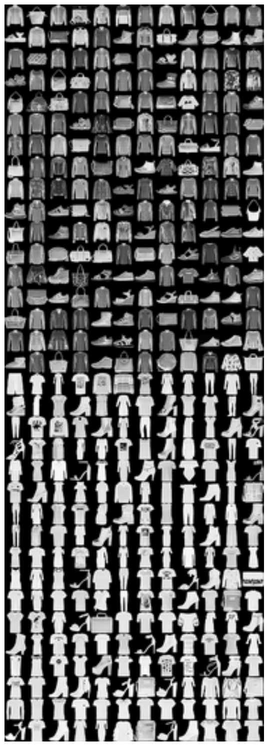
(d) $t_0 = 0.8$.

Figure 24: The 204 smallest (top) and 204 largest (bottom) FMNIST FLIPD estimates with MLP evaluated at different t_0.

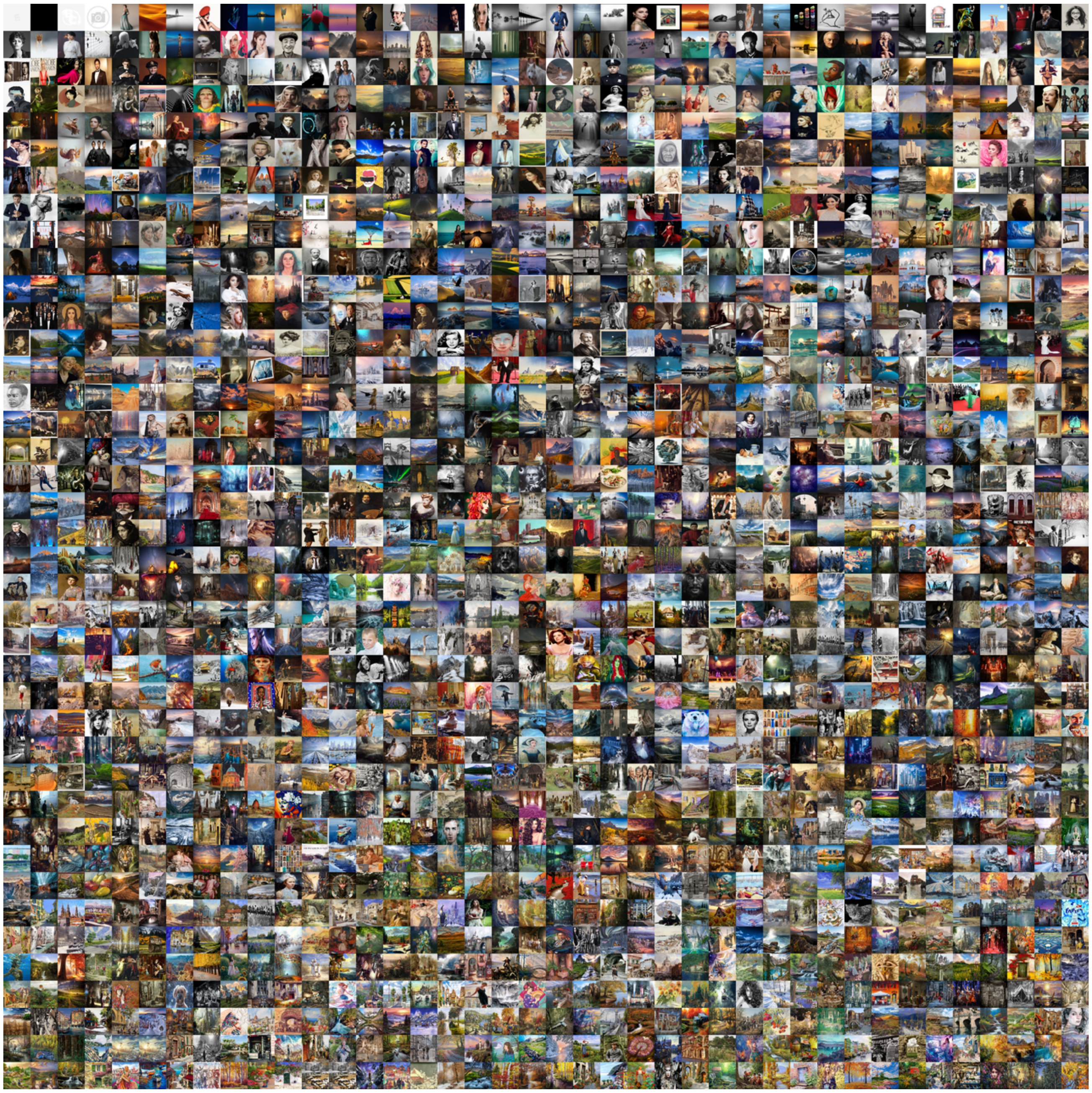

Figure 25: 1600 images from LAION-Aesthetics-625K, sorted by FLIPD estimates with $t_0 = 0.3$.

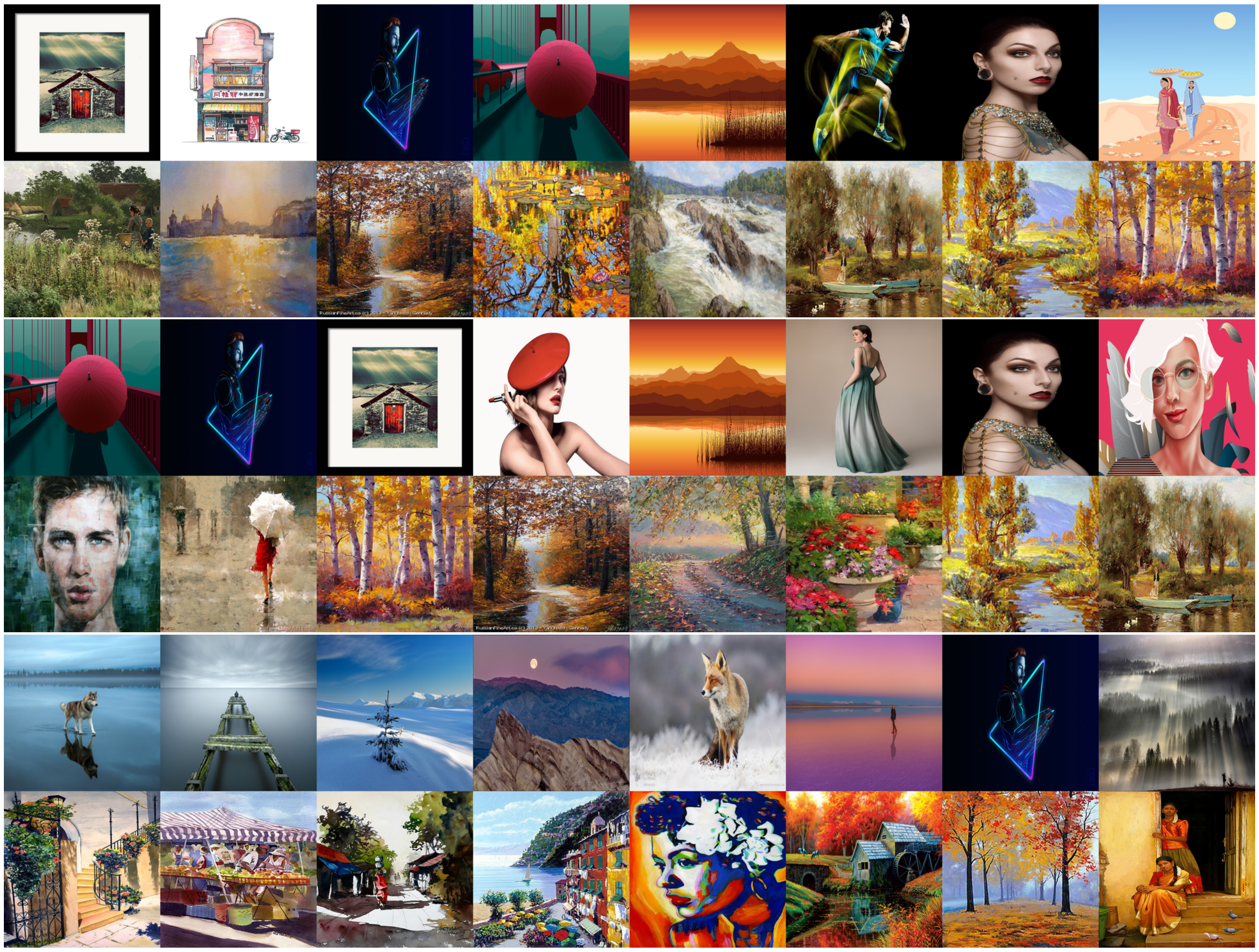

Figure 26: The 8 lowest- and highest-FLIPD values out of 1600 from LAION-Aesthetics-625k evaluated at $t_0 \in \{0.01, 0.1, 0.8\}$. Placeholder icons or blank images have been excluded from this comparison.